Uncertainty-aware modelling of climate-driven transmission suitability for cutaneous leishmaniasis in North Africa

Komi M. Agboka[1,2,*], Souleymane Diallo[1], Steve B.S. Baleba[1,3], Iman B. Hassaballa[1,4], Quinto Juma Meltus[1], Allan M. Ngángá[1], Harriet W. Wangu[1], Khalid Ahmed[5], Chrysantus M. Tanga[1], Tobias Landmann[1], and Elfatih M. Abdel-Rahman[1,6]

[1] International Centre of Insect Physiology and Ecology (ICIPE), Nairobi, Kenya.
[2] Laboratoire de Recherche en Science et Technologie (LARSI), Département de Génie Informatique (GI), École Polytechnique de Lomé (EPL), Université de Lomé, Lomé, Togo.
[3] Department of Zoology and Entomology, University of Pretoria, Hatfield, South Africa.
[4] Department of Medical Entomology, Faculty of Public & Environmental Health, University of Kordofan, Sudan.
[5] Tropical Medicine Research Institute, Khartoum, Sudan.
[6] School of Agriculture and Science, University of KwaZulu-Natal, Pietermaritzburg, South Africa.

Abstract

In vector-borne disease modelling, combining temperature-sensitive vectorial capacity with population growth dynamics often leads to complex frameworks that are difficult to interpret and operationalize. We propose a biologically grounded yet parsimonious approach that integrates the dominant eigenvalue of a temperature-driven next-generation matrix (λmax) with a relative vectorial capacity (VC^*) function to estimate the seasonal climate-driven transmission risk (Q1; January–March, Q2; April–June, Q3; July–September, Q3; October–December) of zoonotic cutaneous leishmaniasis mediated by *Phlebotomus papatasi* across North Africa. Across multiple composite formulations, robust discrimination and spatial reliability were concentrated almost exclusively in Q3, during which additive model weighting 90% VC^* and 10% λmax achieved the highest overall performance (mean AUC-PR = 0.67 ± 0.09; TSS = 0.54; Boyce = 0.85). Outside Q3, predictive skill deteriorated sharply, indicating that seasonal ecological constraints impose a fundamental limit on model performance that cannot be offset by aggregation strategy alone. Uncertainty-aware mid-century projections under SSP2-4.5 and SSP5-8.5, generated via Monte Carlo propagation of temperature-dependent entomological traits, reveal robust spatial risk patterns but strong seasonal heterogeneity in uncertainty. Paired analyses at 581 endemic sites show highly significant seasonal shifts in climatic suitability in Q1–Q3 (Wilcoxon $p < 0.001$), with consistent increases in Q1, strong decreases in Q2–Q3, and weaker, scenario-dependent changes in Q4. Overlaying climatic suitability with healthcare accessibility further reveals persistent spatial mismatches between ecological risk and health system capacity. Together, these results highlight the value of interpretable, seasonally explicit, and uncertainty-aware frameworks for climate-informed disease risk assessment in data-limited settings.

Keywords

zoonotic cutaneous leishmaniasis; Uncertainty-aware modelling; thermal traits; vectorial capacity; North Africa

Data availability

The data used in this study are secondary and derived from publicly available sources, all of which are fully cited within the article. No new primary datasets were generated. All data processing workflows, analytical scripts, and figure-generation code used to produce the results reported in this study are openly available via GitHub and

Correspondence:
Contact K.M. Agboka at kagboka@icipe.org

Cite this article as:
Agboka, K.M., Diallo, S., Baleba, S.B.S., Hassaballa, I.B., Meltus, Q.J., Ngángá, A.M., Wangu, H.W., Ahmed, K., Tanga, C.M., Landmann, T., & Abdel-Rahman, E.M.
Uncertainty-aware modelling of climate-driven transmission suitability for cutaneous leishmaniasis in North Africa
Socio-Environmental Systems Modelling, vol. 8, 18934, 2026, doi:10.18174/sesmo.18934

Socio-Environmental Systems Modelling
An Open-Access Scholarly Journal
http://www.sesmo.org

have been permanently archived on Zenodo: KOMI MENSAH AGBOKA. (2026). komimensah/Climate-Sensitive-Competence-of-Phlebotomus-papatasi-for-Leishmania-major: v0.0 – ZCL climate risk manuscript (V.0.0). Zenodo. https://doi.org/10.5281/zenodo.18200373.

1. Introduction

Zoonotic cutaneous leishmaniasis (ZCL) remains a major neglected tropical disease in the dry and semi-arid regions of North Africa, the Middle East, and Central Asia (Hotez et al., 2012). Due to the protozoan parasite *Leishmania major*, primarily transmitted by the sand fly *Phlebotomus papatasi*, ZCL results in disfiguring skin sores, with sustained economic and psychosocial impacts on infected individuals and populations (Karmaoui et al., 2022a). Approximately 600,000 to 1 million new cutaneous cases emerge annually, with *L. major* causing a high percentage in endemic nations such as Algeria, Tunisia, Sudan, Iran, and Afghanistan (World Health Organization, 2023). Outbreaks related to conflict, population displacement, and ecological disturbances in recent years, particularly in Libya and Syria, have demonstrated the vulnerability of leishmaniasis transmission to swift environmental changes (Berry & Berrang-Ford, 2016).

Phlebotomus papatasi, a primary vector of ZCL, exhibits pronounced temperature sensitivity across multiple life-history traits, including survival, development rate, biting frequency, and the parasite's extrinsic incubation period (Bozorg-Omid et al., 2025). These traits directly influence transmission dynamics and are fundamental to the concept of vectorial capacity (VC), a metric that quantifies a vector population's potential to transmit a pathogen in a given environment. The classical formulation of VC was established by Macdonald (1957) and operationalized by Garrett-Jones (1964) as:

$$VC(T) = \frac{ma^2 * p^{EIP}}{-\ln(p)},$$

where m is vector density, a is the biting rate, p is daily survival probability, and EIP is the duration of the extrinsic incubation period (Garrett-Jones, 1964; Macdonald, 1957). Because temperature influences each of these components, VC is inherently temperature-dependent and serves as a mechanistic linkage between environmental conditions and transmission potential (Mordecai et al., 2019). Temperature also affects other facets of sand fly ecology, including activity patterns and seasonal abundance, as demonstrated in observational studies of phlebotomine sand fly populations (Halimi et al., 2016).

The classical VC formulation captures the premise that a competent vector population is a prerequisite for transmission: even in the presence of suitable reservoirs and susceptible hosts, transmission cannot occur without a vector capable of sustaining parasite development and host contact (Wilson et al., 2017). However, in its standard form, VC treats vector density and demographic rates as static inputs. This simplification can obscure the dynamic influence of environmental drivers on vector population growth and demography over time, particularly under varying thermal regimes.

Mechanistic approaches that explicitly model the full life cycle of insects using temperature-dependent rate functions have been developed across entomological and ecological disciplines. For example, temperature-driven demographic and phenological models have been applied to insects in agricultural systems to estimate growth potential and population dynamics (e.g., Agboka et al., 2025a,b, 2026; Ndjomatchoua et al., 2024; Rossini, Bruzzone, et al., 2022; Rossini, Contarini, et al., 2021, 2022; Rossini et al., 2019, 2024, 2025; Rossini, Rosselló, et al., 2022; Rossini & Bruzzone, 2025). Despite their utility, such approaches have been underutilized in vector-borne disease modeling, where the integration of detailed demographic processes with transmission dynamics remains limited. One recent study by Agboka et al. (2026) combined temperature-dependent demographic traits with livestock density to infer the risk of ZCL in Sudan; however, this work did not incorporate a mechanistic transmission process and instead relied on vector presence proxies rather than explicit transmission dynamics.

Indeed, both traditional VC formulations and physiologically based population models rely on overlapping temperature-sensitive traits, yet their integration for disease risk prediction has been limited. Existing mechanistic formulations often involve systems of coupled differential equations that are complex to calibrate, sensitive to parameter uncertainty, and computationally intensive to apply across large spatial extents or in real-time epidemiological contexts (Parham & Michael, 2010). Such complexity can limit practical usability in

operational settings, particularly for surveillance, early warning, and public health decision-making in resource-constrained regions.

Therefore, we develop a trait-based, climate-driven framework that integrates vector population dynamics and transmission potential to assess ZCL risk mediated by *P. papatasi*. Vector population growth is represented using a temperature-dependent system of ordinary differential equations structured into four developmental stages (eggs, larvae, pupae, adults). From this system, we derive a next-generation matrix whose dominant eigenvalue (λmax) quantifies intrinsic population growth potential under thermal forcing. Transmission-related processes are captured through a temperature-sensitive relative VC derived from classical epidemiological theory.

The two components λmax and relative VC are combined into composite suitability indices using multiple aggregation schemes (additive, geometric, harmonic, and multiplicative) and constrained by a reservoir host ecological envelope (rodent suitability) to ensure biological plausibility. For present-day conditions, we use deterministic estimates based on best-fit trait parameters to maximize interpretability and correspondence with observed field patterns. For future climate projections, we explicitly propagate biological uncertainty using Monte Carlo simulation over bootstrapped trait parameters, generating expected, lower, and upper risk envelopes. This distinction allows deterministic maps to represent current realized suitability, while uncertainty-aware projections characterize plausible future risk under climate change. Model performance using deterministic maps is evaluated against a curated database of *L. major* endemic locations using spatially explicit, threshold-free validation metrics. The framework is subsequently applied to mid-century climate projections (SSP2-4.5 and SSP5-8.5) derived from high-resolution WorldClim data to quantify seasonal and spatial shifts in ZCL risk under climate change.

This process-based, coupled modeling system is more than correlation, as it determines the mechanistic drivers of climate-sensitive risk for *L. major*. By simplifying the linkage between vector thermal ecology and the pathogen's transmission potential, this is a biologically realistic tool for forecasting present and future suitability for *L. major* transmission and elucidating its relation to health care facilities. Our approach augments ecological realism and simplicity in predictions of vector-borne disease and is of practical use in public health surveillance, early warning, and climate-adaptive vector control.

2. Methods

This study quantifies the seasonal climate-sensitive transmission risk of *L. major* mediated by *P. papatasi* across its endemic region in North Africa (Figure 1), integrating temperature-dependent vector population dynamics and transmission processes. Analyses were stratified by seasonal quarter, defined as Q1 (January–March), Q2 (April–June), Q3 (July–September), and Q4 (October–December).

The approach integrates vector thermal ecology and the pathogen's transmission potential constrained by a reservoir host ecological envelope to estimate the seasonal risk potential under current (deterministic) and projected (stochastic) climate scenarios (SSP2-4.5 and SSP5-8.5) (Figure 2). Model performance under deterministic conditions was validated using confirmed endemic sites records, and alignment with healthcare access was assessed to explore potential spatial barriers to intervention. All computations were done using R software (R Core Team 2025).

2.1 Trait-driven stage-structured suitability model

The population dynamics of the insect, with the life cycle that could be divided into four life stages: egg (E), larva (L), pupa (P), and adult (A) are governed by the following system of differential equations (Agboka et al., 2025a,b)

$$\begin{aligned} \frac{dE}{dt} &= FA - (D_1 + M_1)E \\ \frac{dL}{dt} &= D_1E - (D_2 + M_2)L \\ \frac{dN}{dt} &= D_2L - (D_3 + M_3)N \\ \frac{dA}{dt} &= D_3N - M_4A \end{aligned} \qquad Eq.(1)$$

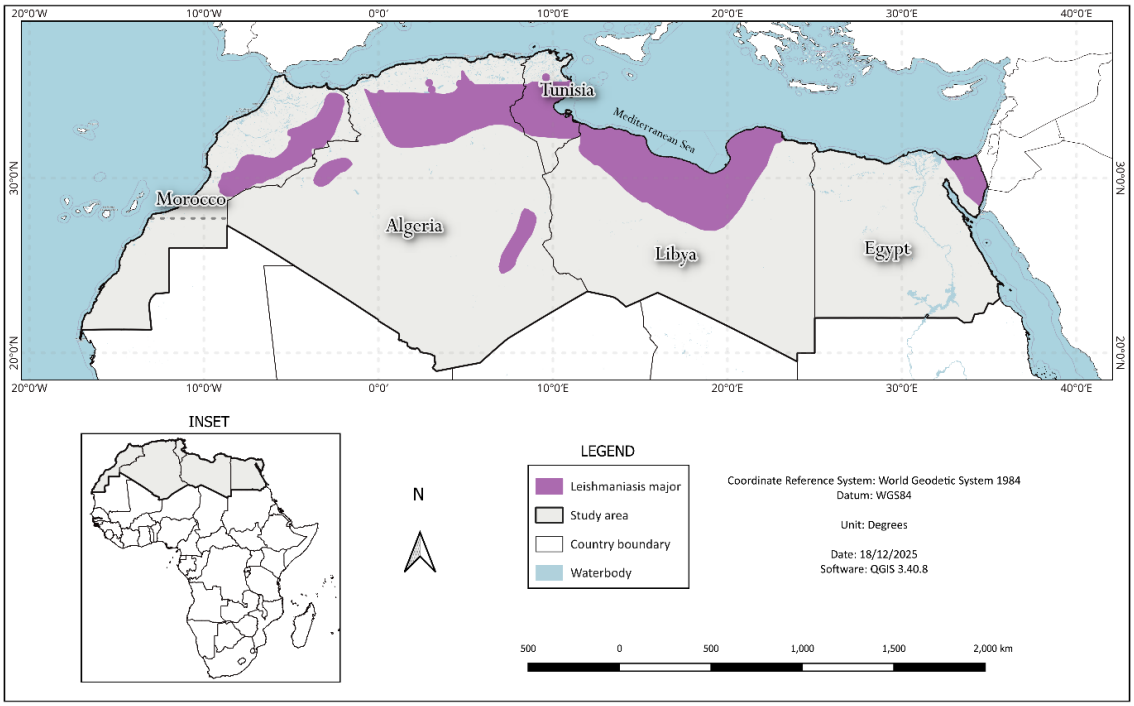

Figure 1: Geographical distribution of *Leishmania major* across North Africa indicating known endemic areas based on compiled records from literature. *Disclaimer: The boundaries, names, and designations used on this map are derived from publicly available shapefiles and do not imply official endorsement or acceptance by the authors or their affiliated institutions. Administrative boundaries were obtained from the Africa Countries dataset (ArcGIS Hub) and are licensed under the Esri Master License Agreement (https://hub.arcgis.com/datasets/africa::africa-countries/about). All raster layers were projected in WGS84 (EPSG:4326).*

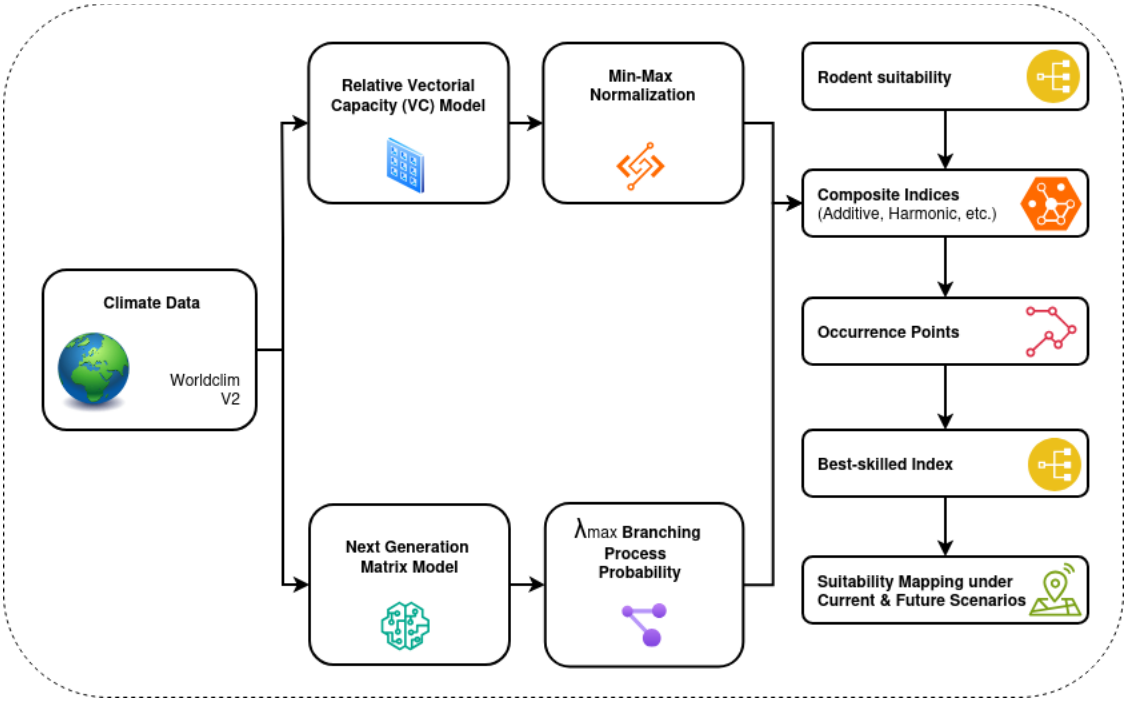

Figure 2: Workflow for constructing climate-sensitive risk indices for *Leishmania major* transmission by *Phlebotomus papatasi*, integrating thermal trait models, vectorial capacity, rodent suitability and climate change scenarios.

The resulting condition for stability can be written as:

$$\frac{F D_E D_L D_P}{(D_E+M_E)(D_L+M_L)(D_P+M_P)M_A} < 1 \qquad Eq.(2)$$

The left-hand side of the equation (2) is the dominant eigenvalue of the next-generation matrix λmax, providing a threshold for population persistence and transmission potential (Diekmann et al., 1990; Van den Driessche & Watmough, 2002) (Supplementary Material A).

$$\lambda max = \frac{F D_E D_L D_P}{(D_E+M_E)(D_L+M_L)(D_P+M_P)M_A} \qquad Eq.(3)$$

Equation (3) indicates sand fly population increase for λmax >1 and a decreasing trend otherwise.

A complete list of the deterministic temperature-dependent transition rates needed in Equation 3 and the corresponding references is retrieved from the cited literature as provided in Table 1.

Table 1: Summary of deterministic temperature-dependent trait functions used to derive λmax for *Phlebotomus papatasi*. All trait functions were parameterized from published laboratory experiments and expressed on a daily (day^{-1}) scale. Development, mortality, and fecundity functions were evaluated within the biologically supported thermal domain of *P. papatasi* and clamped outside the lower and upper thermal thresholds of 17.6 - 35°C (Bozorg-Omid et al., 2025) to avoid extrapolation beyond empirical support. Full parameter values and original data sources are provided.

Variables	Definition	Mathematical expression	Parameter values	Reference of data provenance
$\boldsymbol{F}$	Fecundity rate function (eggs per female per day by the sex ratio)	$a \cdot exp\left\{-\frac{1}{2}\left(\frac{T-T_0}{b}\right)^2\right\}$	a=54.85 T_0=27.7 b=2.31	(Benkova & Volf, 2007; Chelbi & Zhioua, 2007; Yaghoobi-Ershadi et al., 2007)
$\boldsymbol{D_1}$	Development rate function for egg stage Days	$exp\{b_1 + b_2T + b_3T^2\}$	$b_1 = -17.30$ $b_2 = 1.105$ $b_2 = 0.02$	(Kasap & Alten, 2005)
$\boldsymbol{D_2}$	Development rate function for larval stage	$exp\{b_1 + b_2T + b_3T^2\}$	$b_1 = -6.54$ $b_2 = 0.130$	(Kasap & Alten, 2005)
$\boldsymbol{D_3}$	Pupa developmental rate	$exp\{b_1 + b_2T + b_3T^2\}$	$b_1 = -6.98$ $b_2 = 0.17$	(Kasap & Alten, 2005)
$\boldsymbol{M_1}$	Egg mortality rate	$\frac{1}{1 + exp\{k_1 + k_2T + k_3T^2\}}$	k_1=-10 k_2=0.92 k_3=-0.02	(Kasap & Alten, 2005)
$\boldsymbol{M_2}$	Larva mortality rate	$\frac{1}{1 + exp\{k_1 + k_2T + k_3T^2\}}$	k_1=-5.41 k_2=0.26 k_3=-0.002	(Kasap & Alten, 2005)
$\boldsymbol{M_3}$	Pupa mortality rate	$\frac{1}{1 + exp\{k_1 + k_2T + k_3T^2\}}$	k_1=-10 k_2=0.99 k_3=0.02	(Kasap & Alten, 2005)
$\boldsymbol{M_4}$	Adult mortality rate	$\frac{1}{1 + exp\{k_1 + k_2T + k_3T^2\}}$	k_1=3.44 k_2=-0.05 k_3=0.0001	(Benkova & Volf, 2007; Chelbi & Zhioua, 2007; Yaghoobi-Ershadi et al., 2007)

To convert λmax into an interpretable probability of outbreak establishment, we apply a branching-process–based transformation,

$$\lambda max\ norm = \begin{cases} 0 & \lambda max \le 1 \\ 1 - \frac{1}{\lambda max} & \lambda max > 1 \end{cases} \qquad Eq.(4)$$

which estimates the probability that an introduced vector population avoids extinction. This formulation is justified under early-invasion conditions where stochastic dynamics dominate, and density dependence is negligible and remains valid when λmax is defined via the dominant eigenvalue of a structured model (Thompson et al., 2020). Similar eigenvalue-to-probability mappings have recently been applied in sand fly ecological and epidemiological modelling frameworks (Agboka et al., 2025a).

2.2 Vectorial capacity computation

To characterize the thermal sensitivity of *L. major* transmission potential by *P. papatasi*, we simplified the classical VC framework (Macdonald, 1957), which integrates key entomological traits that govern pathogen transmission dynamics. The classical VC equation is as follows:

$$VC(T) = \frac{ma^2 * p^{EIP}}{-\ln(p)} \qquad Eq.(5)$$

Equation 5 is based on the classical vectorial capacity framework, which assumes a single epidemiologically dominant host and homogeneous biting, such that transmission is defined per infectious host (e.g., humans in malaria), with the vector-to-host ratio m explicitly referring to vectors per host (Brady et al., 2016; Ceccato et al., 2012). This assumption does not apply to zoonotic systems such as ZCL, where vectors feed on multiple host species, and transmission depends on host community composition and feeding allocation rather than vector density relative to humans alone (Rizzoli et al., 2019).

We therefore use a relative vectorial capacity index (VC^*), which isolates the temperature dependence of core entomological traits while keeping host factors implicit, to assess climate sensitivity of transmission. The relative vectorial capacity is redefined as follows:

$$VC^* = \frac{a^2 * p^{EIP}}{-\ln(p)} \qquad Eq.(6)$$

We parameterized each component based on empirical and literature-derived parameters (Table 2). Details about inferring biting rate, survival probability, and the EIP from published literature are reported in the Supplementary Material B.

Table 2: Deterministic temperature-dependent entomological components used to derive the relative vectorial capacity (VC^*) for *Phlebotomus papatasi*. All parameters shown are derived exclusively from laboratory-based experiments and are expressed on a daily (day^{-1}) time scale. All quantities represent intrinsic physiological responses of the vector under contr olled conditions. Parameter sources and experimental origins are detailed in Table 2.

Variables	Definition	Mathematical expression	Parameter value	Data source
$\boldsymbol{a}$	Daily biting rate (bites per fly per day)	Constant	0.20	(Parkash et al., 2021)
$\boldsymbol{p}$	Daily survival probability	$1 - \frac{1}{1 + exp\{k_1 + k_2 T + k_3 T^2\}}$	k_1=3.44 k_2=-0.05 k_3=0.0001	(Benkova & Volf, 2007; Lawyer et al., 1990)
$\boldsymbol{EIP}$	Extrinsic incubation period (in days)	$a \cdot exp\left\{-\frac{1}{2}\left(\frac{T - T_0}{b}\right)^2\right\}$	a=7.80 T_0=24.74 b=3.03	(Benkova & Volf, 2007; Chelbi & Zhioua, 2007; Yaghoobi-Ershadi et al., 2007)

To enable direct integration with the normalized λmax scores, the relative vectorial capacity values were normalized using the min–max approach (Hand, 2007), as follows:

$$VC^* norm = \frac{VC^* - VC^* min}{VC^* max - VC^* min} \qquad Eq.(7).$$

2.3. Climate data used in the spatial projection of the dominant eigenvalue and the relative vectorial capacity

To generate spatial projections of λmax and VC^*, we retrieved present-day and mid-century (circa 2050) monthly temperature projections from the WorldClim database accessed in January 2026 (Fick & Hijmans, 2017). Both near-current and future climate conditions were represented using the SSP2-4.5 and SSP5-8.5 scenarios. To reduce bias associated with reliance on a single general circulation model (GCM), we selected three GCMs, viz. EC-Earth3-Veg, IPSL-CM6A-LR, and UKESM1-0-LL, which have previously demonstrated strong performance over North Africa (Babaousmail et al., 2021).

For each scenario, we constructed a multi-model ensemble by averaging projections across the selected GCMs with equal weighting, thereby reducing inter-model variability and producing more robust climate inputs. To capture seasonal temperature dynamics relevant to vector and pathogen development, monthly outputs were aggregated into biologically meaningful seasonal periods (e.g., January–March, April–June etc.). These seasonal temperature summaries were subsequently used to drive the temperature-dependent transmission framework, enabling direct combination of λmax and VC^*, under current and mid-century climate conditions.

2.4. Composite indices formulation

To generate a robust spatial risk of *L. major* under climate-sensitive scenarios, we derived and tested four mathematical combinations of the two mechanistic risk components λmax and VC^* as follows:

- Geometric Mean:

$$GM = \sqrt{\lambda max\ norm * VC^*\ norm} \qquad Eq.(8).$$

- Harmonic Mean:

$$\mathrm{HM} = \frac{2*(\lambda max\ norm * VC^*\ norm)}{(\lambda max\ norm + VC^*\ norm)} \qquad Eq.(9).$$

- Additive composite (weighted mean). We combined the two probability surfaces using a convex weighted mean:

$$AM = w_1 * \lambda max\ norm + w_2 * VC^*\ norm,\ w_1, w_2 \in [0,1], w_1 + w_2 = 1\ Eq.(10).$$

To evaluate sensitivity to relative emphasis on population growth versus transmission, we explored a discrete weight grid with a step of 0.1:

$(w_1, w_2) \in \{(0.9,0.1), (0.8,0.2), \ldots\ldots, (0.1,0.9)\}$. For clarity, additive models are denoted using the shorthand additiveX, where X indicates the percentage weight assigned to λmax. For example, additive10 corresponds to 10 % $\lambda max\ norm$, and 90 % $VC^*\ norm$, and so on up to additive90.

- Multiplicative Index:

$$MUL = \lambda max\ norm \times VC^*\ norm \quad Eq.(11).$$

2.5. Deterministic present-day mapping and uncertainty-aware future projections

Present-day (baseline) maps of the normalized λmax and VC^* were generated using the single optimum parameter set from the fitted thermal trait functions (Tables 1 and 2) (i.e., best-fit coefficients for development, mortality, fecundity, and EIP). This deterministic configuration was used to provide a clear and reproducible baseline representation of current suitability. Future projections explicitly accounted for biological parameter uncertainty using a two-stage Monte Carlo framework.

First, each thermal trait function was refit using parametric bootstrap resampling (n = 500 resamples per trait) from the underlying experimental datasets. Bootstrap refits that failed numerical convergence were discarded, and only successful refits were retained. Second, uncertainty was propagated through the full mechanistic

pipeline using Monte Carlo sampling (n = 1,000 realizations). In each realization, one parameter set was independently sampled from each trait's bootstrap distribution and propagated through (i) the λmax and (ii) the VC^* formulation. For each temperature, we summarized outputs by the posterior mean and 95% interval (2.5th–97.5th percentiles), and defined uncertainty upper and lower difference. Uncertainty was also propagated to composite risk surfaces by recomputing each composite formulation for every Monte Carlo draw, then summarizing each grid cell and quarter using the posterior mean and 95% interval. This preserves nonlinear interactions between λmax , and VC^*, yielding spatially explicit uncertainty-aware risk maps.

Structural uncertainty across general circulation models (GCMs) was not explicitly propagated. Climate forcing was represented by the median ensemble across three GCMs per scenario, providing a single representative trajectory for each SSP. SSPs were therefore treated as scenario pathways (not probabilistic realizations), and results were reported separately for SSP2-4.5 and SSP5-8.5. All simulations used a fixed random seed to ensure reproducibility.

2.6. Ecological envelope of rodent hosts

In addition to λmax and VC^*, we explicitly accounted for ecological envelope (*Meriones shawi*, *Psammomys obesus*,) under present and future climate (SSP2-4.5 and SSP5-8.5), representing the environmental suitability for rodent reservoir presence following the methodology described by Agboka et al. (2025b). This layer was incorporated as a multiplicative modifier of the composite risk index to ensure that elevated vector and insect suitability translated into risk only where reservoir hosts are ecologically plausible. Rodent occurrence records were compiled using *rgbif* package GBI (Chamberlain & Boettiger, 2017), subjected to basic geographic quality control, and treated as presence-only data. Candidate environmental predictors that are relevant to rodent suitability included the Global Aridity Index (Zomer et al., 2022), Normalized Difference Vegetation Index (NDVI) (Huete et al., 1999), and soil texture (Hengl et al., 2015), Land used land cover (Hou et al., 2022), and temperature (section 2.3), capturing complementary constraints on moisture availability, vegetation productivity, and substrate conditions relevant to rodent habitat persistence (Hua et al., 2025; Karmaoui et al., 2022b).

While localized land degradation may occur, soil texture represents a relatively stable edaphic constraint and is not expected to change substantially at regional scales over the present–mid-century period considered here. All data links and accessed dates are provided in Supplementary Material C. NDVI exhibited strong correlation with the aridity index and was therefore excluded, as Global-AI already captures long-term moisture and vegetation constraints over a climatological period with existing future scenarios consistent with the temperature ensemble inputs. Soil texture was held constant across future scenarios due to the absence of robust projections. The remaining predictors were used to train an ensemble species distribution model (SDM) comprising generalized linear models (GLM), generalized additive models (GAM), and random forests (RF) under a five-fold cross-validation framework. Ensemble predictions were generated using performance-weighted averaging based on AUC (Area Under the Receiver Operating Characteristic Curve) and TSS (True Skill Statistic), yielding a continuous rodent suitability surface ranging from 0 (unsuitable) to 1 (highly suitable) (Supplementary Material C, Figure C.1).

2.7. Model skill assessment and index selection (deterministic present-day)

To evaluate predictive skill and identify the most reliable composite index for mapping *L. major* environmental risk, we compiled georeferenced endemic records across North Africa from published secondary sources (Aoun and Bouratbine 2014; Karmaoui et al. 2022a). We retained only locations explicitly attributed to *L. major* transmitted by *P. papatasi* (n = 673); records lacking etiological attribution were excluded.

Model evaluation was conducted using present-day deterministic risk surfaces. To generate background locations, we implemented an environmentally stratified sampling design over the accessible area, defined as the regional boundary after excluding a buffer around presences (100 km). Environmental strata were constructed by quantile binning of representative predictors, and background points (n = 1000) were sampled to ensure balanced coverage across strata. Where specified, sampling within strata was weighted by a population bias surface (source from https://data.humdata.org/organization/worldpop, at 1km resolution and accessed in January 2026) to account for heterogeneous observation effort while preserving environmental coverage.

Predictive performance was assessed using spatially blocked cross-validation (block radius 100 km; 5 folds; 100 randomizations), with all metrics computed on withheld blocks. Discrimination and spatial reliability were quantified using the area under the precision–recall curve (AUC-PR) and partial ROC ratios, evaluated at low false-positive rates (FPR ≤ 0.10, where FPR is the proportion of true absences incorrectly predicted as presences), and the continuous Boyce index. Thresholds were introduced solely for TSS estimation: within each fold, the cutoff that maximized TSS was computed and used exclusively to report TSS, not to produce binary predictions. Calibration was assessed using binned reliability curves, summarized by the calibration slope across folds.

2.8. Projected mid-century changes in climatic suitability at endemic

Leshmania major sites were quantified using paired, non-parametric statistical tests. For each seasonal quarter (Q1–Q4) and emissions scenario (SSP2-4.5 and SSP5-8.5), climatic suitability values were extracted for 581 endemic locations under present-day conditions and under future projections. Analyses were conducted on paired differences (future − present) at identical locations to preserve spatial correspondence and avoid pseudo-replication. Although 673 georeferenced locations were available in the curated dataset, not all overlapped with valid climatic suitability raster cells. Locations with missing suitability values under either present-day or future conditions were excluded. Consequently, 581 sites with complete paired present–future estimates were retained for all statistical analyses. Departures from present-day suitability were evaluated using the paired Wilcoxon signed-rank test (Woolson, 2008), testing the null hypothesis that the median paired difference equals zero. This test was selected because the suitability values are bounded and do not satisfy normality assumptions. P-values were computed using the normal approximation given the large sample size, and statistical significance was assessed at $\alpha = 0.05$.

Uncertainty was propagated at both the climate-projection and statistical-inference levels. Future suitability was derived from ensemble-based projections, including mean, lower, and upper bounds, which capture uncertainty arising from climate model variability. This uncertainty is reflected in the distribution of paired suitability changes across endemic sites and visualized using violin and box plots. To quantify uncertainty in the magnitude of change, effect size was measured using the matched rank-biserial correlation (r_{rb}), a direction-sensitive, scale-free metric appropriate for paired non-parametric data. Ninety-five percent confidence intervals for r_{rb} were estimated via non-parametric bootstrap resampling (500 resamples of paired observations), recalculating r_{rb} for each resample and extracting the 2.5th and 97.5th percentiles of the resulting distribution.

2.9. Population-stratified analysis of suitability-healthcare accessibility

To evaluate spatial equity in disease vulnerability, we quantified the relationship between modeled climatic suitability and access to healthcare facilities using a distance-based approach, explicitly conditioning the analysis on human population distribution. Healthcare access points for individual countries (Morocco, Tunisia, Egypt, and Libya) were spatially joined into a single shapefile. Euclidean distance (km) to the nearest health facility was calculated from these georeferenced facility locations obtained from the Humanitarian Data Exchange (HDX; https://data.humdata.org/). Health facility datasets were accessed in January 2026 and correspond to the most recent publicly available facility layers for North Africa at the time of data retrieval. Moreover, Health facility datasets are known to under-represent informal, private, and mobile health services, and may underestimate access in rural areas; however, this bias is largely spatially structured and therefore unlikely to reverse relative accessibility gradients at the regional scale. Facility point locations were therefore rasterized and used to compute continuous pixel-level distance-to-facility surfaces, expressed in kilometers. Distance rasters were spatially aligned to the climatic suitability surfaces using bilinear resampling to ensure identical resolution, extent, and grid geometry. This metric captures relative geographic accessibility to healthcare infrastructure rather than realized healthcare utilization.

Gridded population density data were harmonized to the same spatial resolution and extent and used as a spatial filter rather than a weighting factor for simplicity. Specifically, population density was employed to delineate analysis domains corresponding to increasing levels of human presence, thereby restricting inference to areas where human exposure and healthcare access are epidemiologically meaningful. Population values were not used to weight correlations or raster values; instead, they determined which pixels were included in each analysis.

To assess the robustness of suitability–access relationships across gradients of human settlement, analyses were repeated under progressively stricter population density thresholds (≥1, ≥5, ≥10, ≥25, ≥50, and ≥100 persons km^{-2}). Lower thresholds retain sparsely populated regions, while higher thresholds increasingly focus the analysis on densely inhabited areas. This stratified approach avoids reliance on a single arbitrary population cutoff and allows explicit evaluation of how inferred relationships change as attention shifts from marginal landscapes to population centers. For each population threshold, only pixels meeting the criterion were retained, and associations between climatic suitability and healthcare distance were computed on the filtered raster domain. Linear associations were quantified using Pearson correlation coefficients, with uncertainty estimated via non-parametric bootstrap resampling (500 iterations) to derive 95% confidence intervals. In parallel, Spearman rank correlations were computed to assess robustness to non-linearity and the presence of tied values inherent to gridded raster data. This population-stratified framework enables transparent assessment of how healthcare accessibility disparities co-vary with climatic suitability under increasing population concentration, while avoiding conflation of environmental risk patterns with uninhabited or weakly populated areas.

In addition, bivariate maps were constructed by jointly classifying climatic suitability and healthcare accessibility into three ordinal categories (low, medium, high; and good, moderate, poor, respectively) using tercile-based thresholds derived from their empirical distributions within the population-masked domain (≥1 person·km^{-2}). A tercile-based classification was adopted to provide a scale-independent, data-driven representation of relative risk and accessibility, avoiding arbitrary absolute cut-points while preserving spatial contrasts relevant for public-health prioritization. This approach highlights spatial co-occurrence patterns and identifies priority zones where high climatic suitability coincides with poor healthcare access, which are most relevant for targeted surveillance and intervention.

3. Results

3.1. Model robustness

Model performance exhibited a pronounced seasonal structure, with predictive skill concentrated almost exclusively in the third quarter (Q3). Across all composite formulations and evaluation metrics, discrimination, threshold-based accuracy, and spatial reliability declined substantially in Q2 and collapsed in Q1 and Q4, indicating that seasonal signal strength dominated model performance more strongly than aggregation strategy. In Q3, additive composite formulations consistently outperformed non-additive alternatives, with the additive10 model emerging as the best-performing configuration. This formulation achieved moderate discrimination under strong class imbalance (mean AUC-PR = 0.67 ± 0.09; 95% CI: 0.59–0.75), robust threshold-based accuracy (mean TSS = 0.54; 95% CI: 0.46–0.61), high sensitivity at low false-positive rates (pROC > 4), and strong spatial reliability (Boyce = 0.85). Closely related additive formulations (additive20 and additive30) retained good performance but exhibited a progressive trade-off between discrimination and spatial ranking consistency.

In contrast, harmonic, geometric, and multiplicative composites showed consistently weaker discrimination and threshold-based accuracy, with the multiplicative formulation performing poorly across all metrics even during Q3. Outside Q3, predictive skill deteriorated sharply for all models: Q2 predictions were characterized by increased uncertainty and reduced spatial reliability, while Q1 and Q4 predictions converged toward near-random discrimination, negligible TSS, and non-informative or negative Boyce indices. Collectively, these results demonstrate that only additive composite models evaluated during Q3 provide a combination of discrimination, calibration, and spatial reliability sufficient for interpretation, with additive10 offering the most robust balance of predictive performance. The systematic failure of all formulations outside this seasonal window confirms that seasonal ecological constraints impose a fundamental limit on predictive skill that cannot be compensated for by composite structure alone. The summarized results of the best-performing composite models are presented in Table 3, representing a top-performing subset dominated by Q3 and, to a lesser extent, upper-Q2 models, while poorly performing Q1 and Q4 models are excluded and reported in Supplementary Material D.

Table 3: Performance of the best-performing composite models, representing a top-performing subset of the composite risk indices across quarters and aggregation methods. Model skill is summarized using AUC-PR (mean ± SD with 95% confidence intervals), TSS, partial ROC (pROC), and the Boyce index.

Method	Quarter	AUC-PR (mean ± SD, 95% CI)	TSS (95% CI)	pROC (95% CI)	Boyce
additive10	Q3	0.67 ± 0.09 (0.59–0.75)	0.54 (0.46–0.61)	4.52 (4.04–5.01)	0.85
additive20	Q3	0.58 ± 0.10 (0.49–0.67)	0.40 (0.34–0.45)	2.89 (2.28–3.50)	0.91
additive30	Q3	0.50 ± 0.12 (0.40–0.60)	0.35 (0.30–0.41)	1.80 (1.23–2.37)	0.60
harmonic	Q3	0.49 ± 0.10 (0.41–0.58)	0.24 (0.16–0.32)	2.33 (2.02–2.64)	0.71
geometric	Q3	0.46 ± 0.11 (0.36–0.56)	0.23 (0.18–0.28)	1.75 (1.15–2.35)	0.37
multiplicative	Q3	0.40 ± 0.09 (0.32–0.48)	0.19 (0.13–0.25)	1.29 (0.78–1.80)	0.31
additive10	Q2	0.53 ± 0.14 (0.41–0.66)	0.39 (0.33–0.45)	2.62 (1.05–4.19)	0.49
additive20	Q2	0.50 ± 0.14 (0.38–0.62)	0.32 (0.27–0.37)	2.63 (1.45–3.81)	0.61
additive30	Q2	0.48 ± 0.12 (0.37–0.58)	0.24 (0.18–0.29)	2.72 (1.47–3.97)	0.52
harmonic	Q2	0.36 ± 0.11 (0.26–0.46)	0.09 (0.01–0.18)	1.85 (0.55–3.16)	0.05
geometric	Q2	0.37 ± 0.12 (0.26–0.47)	0.10 (0.01–0.19)	1.96 (0.50–3.41)	0.34
multiplicative	Q2	0.33 ± 0.11 (0.24–0.43)	0.07 (0.01–0.13)	1.50 (0.44–2.57)	0.06
harmonic	Q4	0.23 ± 0.07 (0.17–0.29)	≈ 0	0.17 (−0.05–0.38)	0.00
multiplicative	Q4	0.26 ± 0.06 (0.20–0.31)	≈ 0	0.11 (−0.04–0.26)	−0.01

3.2. Seasonal patterns of climate-driven *Leishmania major* transmission risk

The deterministic composite risk maps reveal a strong and coherent seasonal structure in climate-driven suitability for *L. major* transmission across North Africa (Figure 3). During Q1, suitability is generally low across the region, with moderate values restricted to Mediterranean coastal zones of Morocco, northern Algeria, and Tunisia. Inland and hyper-arid regions exhibit minimal suitability, reflecting suboptimal temperatures for sand fly development and population growth. In Q2, risk expands markedly both spatially and in magnitude. Moderate to high suitability emerges across northern Algeria, Tunisia, and coastal Libya, corresponding to temperatures approaching the optimal thermal range for *P. papatasi* development, survival, and early seasonal population amplification. Q3 represents the peak transmission season, characterized by the highest and most spatially extensive suitability across North Africa. Large contiguous areas of Algeria, Tunisia, Libya, and eastern Morocco exhibit elevated risk, indicating sustained climatic conditions favorable for vector population persistence and transmission potential. This quarter consistently aligns with the strongest model skill, supporting its epidemiological relevance. In Q4, suitability declines and contracts spatially, though residual risk persists in climatically buffered inland regions, particularly in central Algeria and parts of Tunisia and Libya. Coastal areas exhibit more rapid declines, consistent with seasonal cooling and reduced vector performance.

Across all quarters, the deterministic composite risk index displays spatial patterns that are ecologically consistent with the known biology of *P. papatasi* and the ecology of *L. major* reservoir hosts. Persistent risk cores are concentrated in semi-arid and steppe regions, while extremely arid Saharan zones remain unsuitable despite high temperatures, reflecting ecological constraints beyond thermal permissiveness. Mediterranean coastal regions show a moderated risk, particularly during summer, consistent with lower peak temperatures and humidity regimes less favorable for sustained transmission.

3.3. Climate changes and endemicity of *Leishmania major*

Figure 4 presents uncertainty-propagated mid-century projections of *L. major* transmission risk under the SSP2-4.5 scenario, summarized as lower-bound, posterior mean, and upper-bound realizations of the composite risk index for each seasonal quarter (Q1–Q4). Unlike the deterministic projection, which represents a single best-fit parameter set, these maps capture parameter-driven uncertainty arising from temperature-dependent vector traits governing population growth and relative vectorial capacity. Across all seasons, the posterior mean surfaces closely resemble the deterministic risk maps, indicating that the spatial structure of transmission suitability is largely governed by robust climatic gradients rather than parameter noise. This agreement confirms that the deterministic model provides a reasonable central estimate of present-day risk. However, the lower- and upper-bound maps reveal substantial heterogeneity in uncertainty, both spatially and seasonally. During

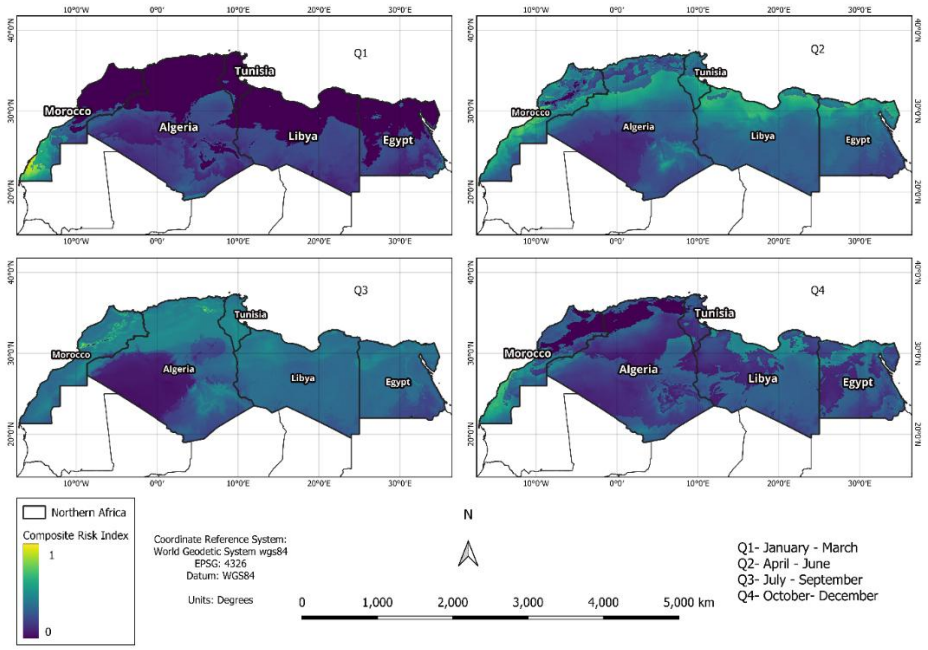

Figure 3: Seasonal distribution of climate-driven *Leishmania major* transmission risk in North Africa. Seasonal maps of the deterministic composite risk index for *Leishmania major* transmission mediated by *Phlebotomus papatasi* across North Africa under present-day climatic conditions. Risk surfaces are shown for four quarters: Q1 (January–March), Q2 (April–June), Q3 (July–September), and Q4 (October–December). Values are scaled from low (blue) to high (purple) climatic suitability. (See Disclaimer in footnote[1])

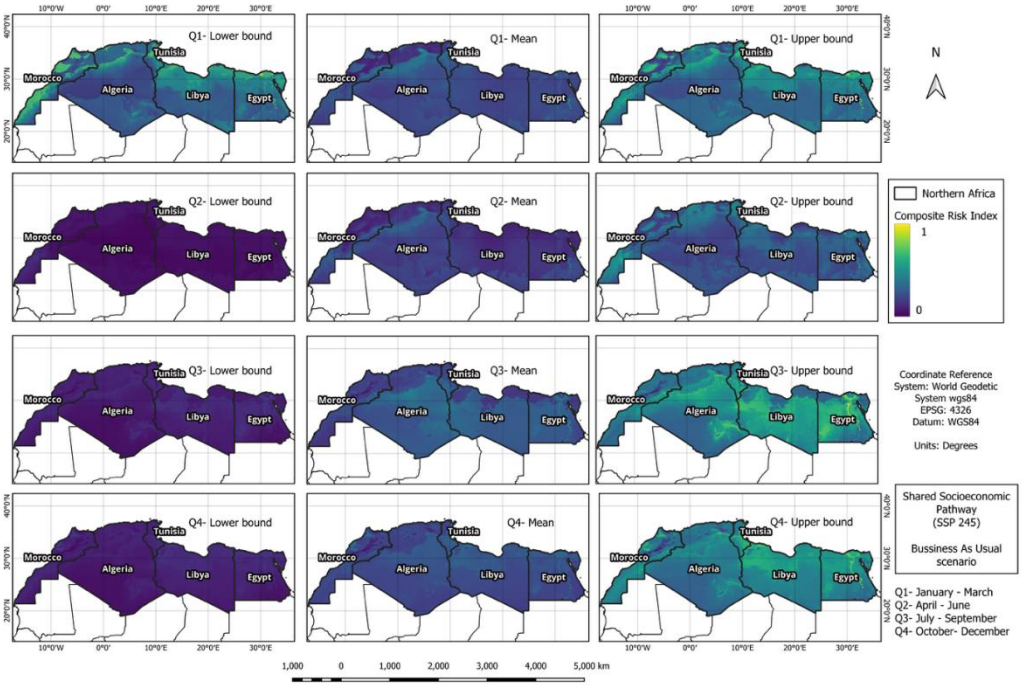

Figure 4: Uncertainty-aware seasonal projections of *Leishmania major* transmission**.** Seasonal stochastic projections of *Leishmania major* transmission risk mediated by *Phlebotomus papatasi* across North Africa under SSP2-4.5 climatic conditions. For each quarter (Q1–Q4), maps show the lower bound (2.5th percentile), posterior mean, and upper bound (97.5th percentile) of the composite additive risk index derived from Monte Carlo propagation of temperature-dependent entomological trait uncertainty. (See Disclaimer in footnote[1])

[1] *Disclaimer: The boundaries, names, and designations used on this map are derived from publicly available shapefiles and do not imply official endorsement or acceptance by the authors or their affiliated institutions. Administrative boundaries were obtained from the Africa Countries dataset (ArcGIS Hub) and are licensed under the Esri Master License Agreement (https://hub.arcgis.com/datasets/africa::africa-countries/about). All raster layers were projected in WGS84 (EPSG:4326).*

cooler periods (Q1 and Q4), uncertainty ranges are narrow and spatial patterns are relatively stable, reflecting constrained vector development and survival at suboptimal temperatures. In contrast, warm-season quarters (Q2 and Q3) exhibit markedly wider uncertainty envelopes, particularly across semi-arid and arid regions, where nonlinear thermal responses amplify sensitivity to trait parameter variation. Notably, the upper-bound projections identify areas where transmission suitability could be substantially higher than suggested by deterministic estimates, while the lower-bound projections delineate zones where risk remains low even under favorable biological assumptions.

Figure 5 presents the uncertainty-aware mid-century projections of *L. major* transmission risk under the high-emissions SSP5-8.5 scenario, expressed as lower-bound, posterior mean, and upper-bound realizations of the composite risk index for each seasonal quarter (Q1–Q4). These projections integrate uncertainty in temperature-dependent entomological traits through Monte Carlo propagation while conditioning on SSP5-8.5 climate forcing. Across all seasons, the posterior mean projections indicate a systematic intensification of transmission suitability relative to present-day conditions, with the strongest increases occurring during the warm and transitional quarters (Q2 and Q3). Under SSP5-8.5, thermally favorable conditions expand spatially and temporally, leading to higher mean suitability across much of the region. Uncertainty envelopes widen substantially under this scenario. The upper-bound projections reveal extensive areas where transmission suitability reaches high levels during Q2–Q4, reflecting the compounding effects of elevated temperatures on vector development, survival, and biting activity. In contrast, the lower-bound projections retain heterogeneous patterns, indicating that even under strong warming, unfavorable biological parameter combinations may locally constrain transmission potential. Seasonal contrasts are particularly pronounced. During cooler quarters (Q1 and Q4), uncertainty remains comparatively moderate, whereas Q2 and Q3 exhibit both the highest mean suitability and the widest uncertainty ranges, highlighting nonlinear amplification of biological uncertainty under extreme warming.

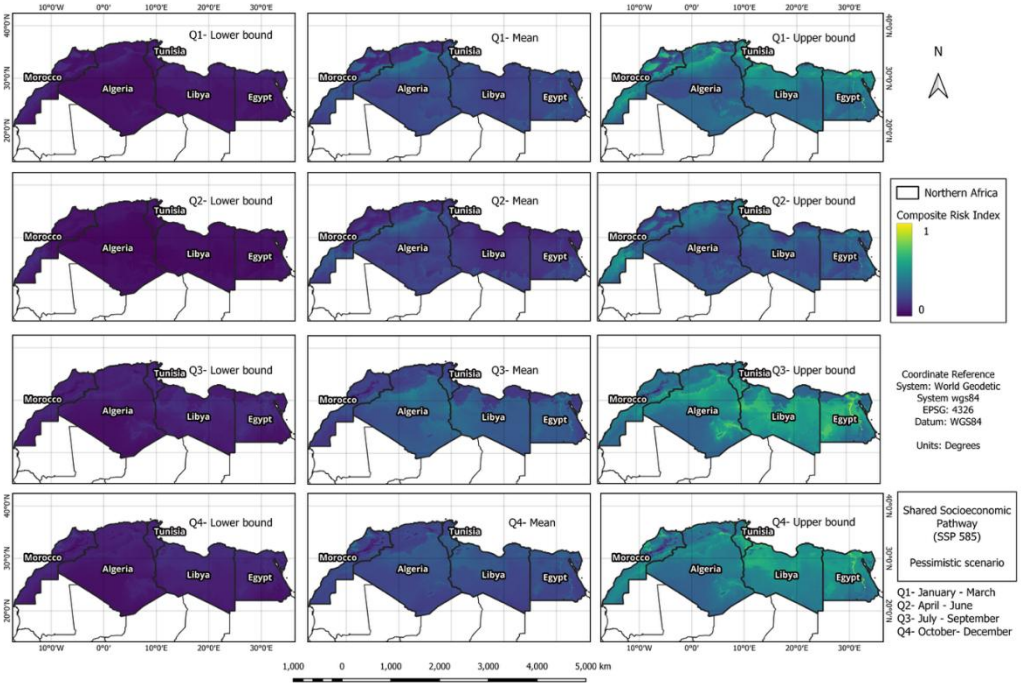

Figure 5: Uncertainty-aware seasonal projections of *Leishmania major* transmission**.** Seasonal stochastic projections of *Leishmania major* transmission risk mediated by *Phlebotomus papatasi* across North Africa under SSP5-8.5 climatic conditions. For each quarter (Q1–Q4), maps show the lower bound (2.5th percentile), posterior mean, and upper bound (97.5th percentile) of the composite additive risk index derived from Monte Carlo propagation of temperature-dependent entomological trait uncertainty. (See Disclaimer in footnote[2])

[2] *Disclaimer: The boundaries, names, and designations used on this map are derived from publicly available shapefiles and do not imply official endorsement or acceptance by the authors or their affiliated institutions. Administrative boundaries were obtained from the Africa Countries dataset (ArcGIS Hub) and are licensed under the Esri Master License Agreement (https://hub.arcgis.com/datasets/africa::africa-countries/about). All raster layers were projected in WGS84 (EPSG:4326).*

3.4. Seasonal changes in climatic suitability at endemic sites

Projected mid-century climatic suitability for *L. major* differed markedly from present-day conditions across most seasonal quarters, with clear shifts in the distribution of paired suitability changes at endemic sites (Figure 6). Using a paired Wilcoxon signed-rank test that explicitly accounted for within-site comparisons at the same 581 endemic locations, we detected highly significant shifts in suitability for both SSP2-4.5 and SSP5-8.5 scenarios in quarters Q1–Q3 (all $p < 0.001$; Table 4).

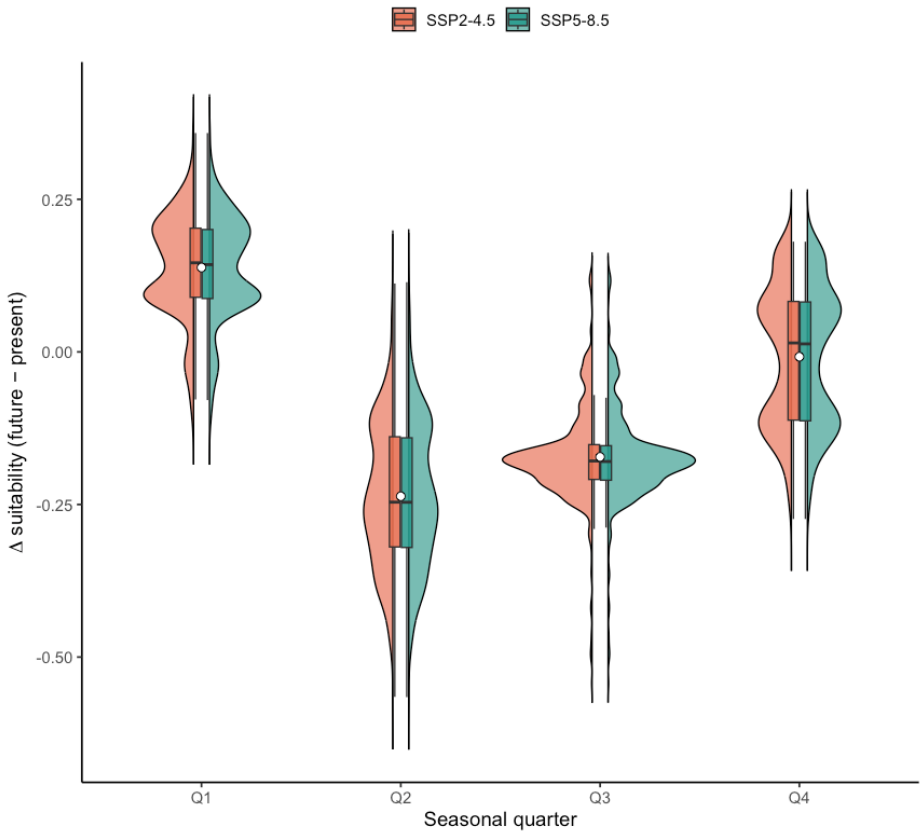

Figure 6: Distribution of projected changes in climatic suitability (Δ-suitability = future − present) at endemic *Leishmania major* sites across seasonal quarters. Violins show the full distribution of paired site-level changes, incorporating stochastic uncertainty from future climate projections (lower, mean, and upper estimates). Boxes indicate the interquartile range with median, white points denote the mean, and all values represent paired differences at the same sites (n = 581 per quarter).

Table 4: Paired Wilcoxon signed-rank tests comparing present-day and projected mid-century climatic suitability at endemic *L. major* sites. Tests were conducted using paired differences at the same 581 locations for each seasonal quarter and scenario. Effect size is reported as the matched rank-biserial correlation (r_{rb}) with 95% bootstrap confidence intervals. Positive values indicate increases in suitability relative to present-day conditions, while negative values indicate decreases.

Quarter	Scenario	N sites	p-value	Signif.	r_{rb}	95% CI (low)	95% CI (high)
Q1	SSP2-4.5	581	p < 0.001	***	0.972	0.959	0.983
Q1	SSP5-8.5	581	p < 0.001	***	0.970	0.958	0.983
Q2	SSP2-4.5	581	p < 0.001	***	−0.997	−0.999	−0.994
Q2	SSP5-8.5	581	p < 0.001	***	−0.997	−0.999	−0.994
Q3	SSP2-4.5	581	p < 0.001	***	−0.992	−0.997	−0.985
Q3	SSP5-8.5	581	p < 0.001	***	−0.992	−0.997	−0.985
Q4	SSP2-4.5	581	5.43×10^{-2}	ns	−0.092	−0.188	0.004
Q4	SSP5-8.5	581	3.00×10^{-2}	*	−0.104	−0.201	−0.007

Moreover, effect sizes were consistently large in magnitude, as quantified by the matched rank-biserial correlation (r_{rb}), indicating near-uniform directional changes across sites (Table 4). In Q1, suitability increased markedly under both scenarios (SSP2-4.5: r_{rb} = 0.97, 95% CI [0.96, 0.98]; SSP5-8.5: r_{rb} = 0.97, 95% CI [0.96, 0.98]), consistent with the strong positive displacement of the Δ-suitability distributions (Figure 6). In contrast, Q2 and Q3 exhibited pronounced decreases in suitability, with effect sizes approaching −1 under both scenarios, reflecting highly consistent negative shifts across endemic sites and narrow distributional overlap (Figure 6; Table 4). In Q4, changes in suitability were comparatively modest. Under SSP2-4.5, the effect was small and not statistically significant (p = 0.054), whereas under SSP5-8.5 a weak but significant decrease was detected (r_{rb} = −0.10, 95% CI [−0.20, −0.01]; Table 4). This reduced effect magnitude is reflected in the broader, near-zero-centered Δ-suitability distributions observed for Q4 (Figure 6), suggesting that projected climate change may primarily alter suitability during the first three quarters of the year, with late-season effects being more limited and scenario-dependent.

3.5. Disease risk and the health care system

Table 5 summarizes the sensitivity of the spatial association between modeled climatic suitability and healthcare accessibility across increasing population density thresholds. Using the population density exclusively as a spatial filter, progressively restricting the analysis to increasingly inhabited areas (≥1 to ≥100 persons km^{-2}), a clear and monotonic strengthening of the association is observed. At the lowest threshold (≥1 person km^{-2}; N = 68,338 pixels), the relationship between suitability and distance to healthcare facilities is already positive but moderate (Pearson r = 0.23, 95% CI: 0.22–0.24; Spearman ρ = 0.14), indicating limited but detectable co-location of environmental suitability and healthcare access constraints across sparsely populated regions. As the analysis is progressively restricted to more densely inhabited areas, correlation strength increases substantially. At ≥5 persons km^{-2} (N = 41,307), Pearson r rises to 0.31 (95% CI: 0.30–0.32), with a corresponding increase in rank correlation (ρ = 0.21). This trend continues at ≥10 persons km^{-2} (N = 32,208), where Pearson r reaches 0.34 (95% CI: 0.33–0.35), indicating stronger spatial coupling in moderately populated landscapes.

Table 5: Population-threshold sensitivity of suitability–healthcare association. Pearson correlation coefficients are reported with bootstrap 95% confidence intervals. Spearman's rank correlations are reported with significance levels (*** p < 0.001).

Population threshold (persons km^{-2})	N (pixels)	Pearson r	95% CI (Pearson r)	Spearman ρ	p-value (Spearman)
≥ 1	68,338	0.23	0.22 – 0.24	0.14	***
≥ 5	41,307	0.31	0.30 – 0.32	0.21	***
≥ 10	32,208	0.34	0.33 – 0.35	0.24	***
≥ 25	21,151	0.41	0.40 – 0.42	0.30	***
≥ 50	13,864	0.46	0.45 – 0.47	0.38	***
≥ 100	8,632	0.50	0.49 – 0.52	0.46	***

Beyond ≥25 persons km^{-2} (N = 21,151), the association strengthens markedly. Pearson correlations exceed 0.40 (r = 0.41, 95% CI: 0.40–0.42), with Spearman ρ increasing to 0.30, reflecting increasing alignment between high suitability and limited healthcare access in densely inhabited settings. This pattern intensifies further at ≥50 persons km^{-2} (N = 13,864), where Pearson r reaches 0.46 (95% CI: 0.45–0.47) and Spearman ρ increases to 0.38. The strongest association is observed at the highest population threshold (≥100 persons km^{-2}; N = 8,632), where Pearson r reaches 0.50 (95% CI: 0.49–0.52) and Spearman ρ reaches 0.46, indicating a strong and consistent co-location of high climatic suitability and poorer healthcare accessibility in highly populated areas. Confidence intervals narrow progressively with increasing thresholds, reflecting improved statistical stability as the analysis focuses on densely populated domains.

In addition, the bivariate analysis revealed pronounced spatial mismatches between *L. major* climatic suitability and healthcare accessibility across Northern Africa (Figure 7). Areas of high suitability combined with poor healthcare access were primarily concentrated in inland and arid regions, notably across southern Morocco, central and southern Algeria, interior Libya, and parts of western and southern Egypt. These zones represent priority areas where elevated ecological risk coincides with limited access to health services. Regions characterized by high suitability but moderate to good healthcare access were more spatially restricted and occurred mainly in coastal and peri-urban areas, including northern Morocco, coastal Algeria, and parts of

northern Egypt. In contrast, low suitability with good healthcare access dominated densely populated coastal corridors and major urban centers, reflecting favorable service coverage in areas of reduced ecological risk. Intermediate combinations, particularly moderate suitability with poor or moderate access, formed extensive transitional belts surrounding high-risk zones, suggesting areas where incremental changes in climate suitability or healthcare infrastructure could substantially alter vulnerability profiles.

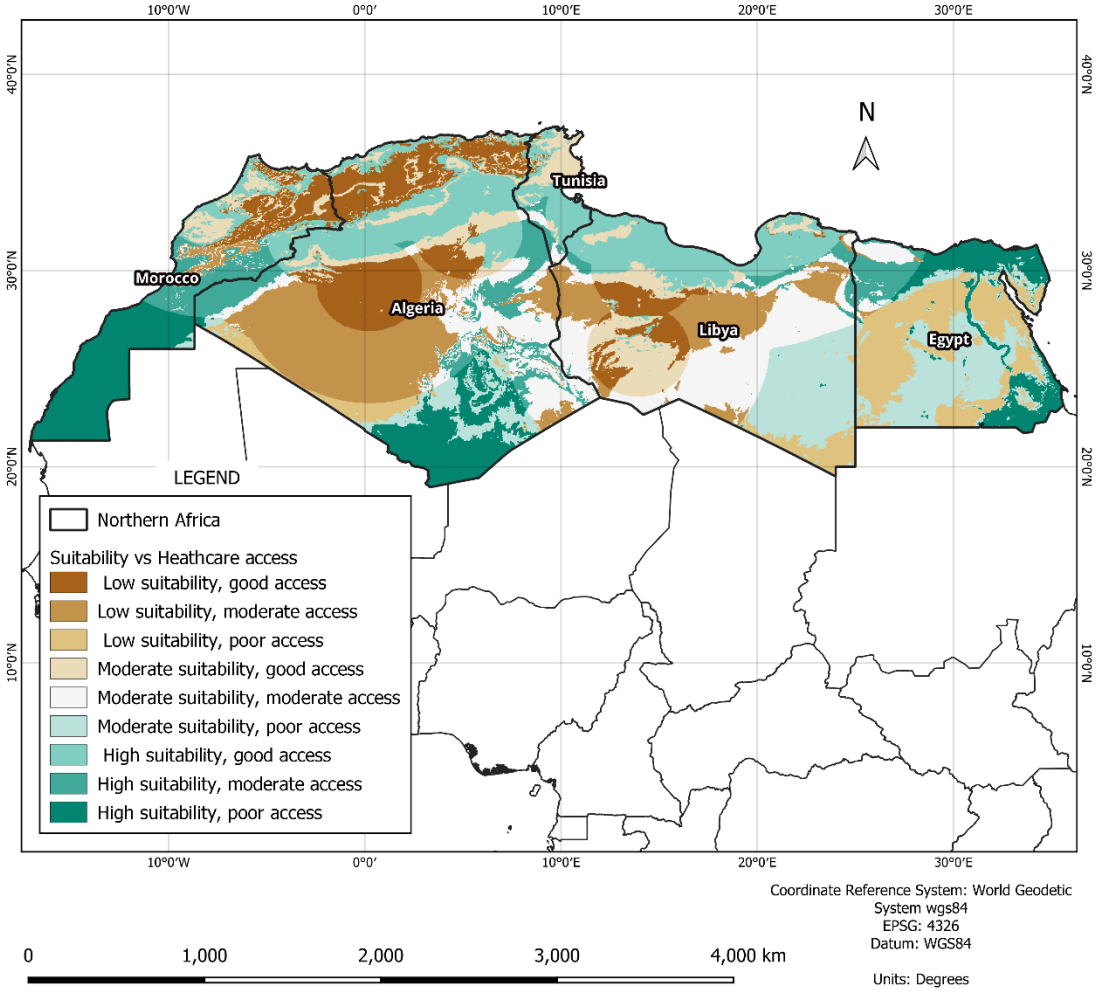

Figure 7: Bivariate classification of *Leishmania major* climatic suitability and healthcare accessibility across Northern Africa. Raster cells represent tercile-based combinations of modeled suitability and distance to the nearest healthcare facility, highlighting areas where high ecological suitability coincides with limited healthcare access. (See Disclaimer in footnote [3])

4. Discussion

4.1. Model

The thermophilic sand fly *P. papatasi* is the primary vector of *L. major*, the etiological agent of ZCL in North African and Middle Eastern arid and semi-arid areas. Its life cycle is restricted by environmental temperature, with thresholds for adult survival (10–35°C) (Bozorg-Omid et al., 2025). The adult female's vectorial capacity is determined by a suite of thermally responsive traits, e.g., biting rate, survival through the EIP, and successful *L. major* development in the midgut (Bates, 2007; Quiñonez-Díaz et al., 2012). Each of these parameter's

[3] *Disclaimer: The boundaries, names, and designations used on this map are derived from publicly available shapefiles and do not imply official endorsement or acceptance by the authors or their affiliated institutions. Administrative boundaries were obtained from the Africa Countries dataset (ArcGIS Hub) and are licensed under the Esri Master License Agreement (https://hub.arcgis.com/datasets/africa::africa-countries/about). All raster layers were projected in WGS84 (EPSG:4326).*

covariates with ambient temperature in nonlinear ways, producing discrete optima for both parasite development and vector competence.

Interestingly, *P. papatasi* also experiences a disconnect between temperatures that are optimal for population growth and those that are optimal for transmission (Bozorg-Omid et al., 2025). For instance, while warmer temperatures accelerate larval development and increase fecundity, they decrease adult lifespan. They can shorten the time available for the completion of the parasites EIP, particularly in marginal environments. This biological discordance between population expansion and pathogen transmission partially accounts for our finding that composite suitability models burdening VC systematically outperformed models weighting λmax in predicting observed ZCL occurrence locations.

Our findings demonstrate that disease risk is best captured when transmission-relevant processes dominate over simple demographic potential. The additive10 composite, which places 90% weight on $VC^*$and only 10% λmax, outperformed λmax -dominant and nonlinear formulations, supporting the idea that environments supporting vector abundance alone may not sustain transmission if vectors do not survive long enough to complete parasite development, making the VC a more direct indicator of transmission competence than a demographic growth rate alone (Brady et al., 2016).

Our results also corroborate the patterns observed in other vector-borne systems. For example, in *Anopheles* mosquitoes and *Aedes spp.*, temperatures for ideal transmission are consistently below temperatures for maximum vector abundance or reproductive potential. Similar results have been reported from dengue, Zika, and West Nile virus models, where temperature optima for pathogen replication and EIP completion differ from those of vector proliferation (Dennington et al., 2024; Suh et al., 2020; Terradas et al., 2024). These trade-offs determine the limits of the transmission niche, a smaller, ecologically restricted space within the larger demographic niche.

Moreover, the study results suggest that climatic conditions during Q3 uniquely satisfy the coupled requirements of transmission competence, high seasonal abundance of *P. papatasi* coinciding with sufficient adult survival to permit parasite development, whereas other quarters may support vector presence without enabling frequent infectious contacts. This interpretation is consistent with North African syntheses showing peak *P. papatasi* densities during the hot season, most commonly between June and September across Algeria, Tunisia, Libya, and Morocco, and with transmission theory demonstrating that vector survival across EIP is a stronger determinant of transmission than vector abundance alone (Karmaoui et al., 2022a).

4.2. Climate warming under uncertainty-aware modelling and intensification of *L. major* transmission risk

Our results show pronounced climate-driven shifts in the seasonal suitability for transmission of *L. major* across its current endemic range, with the direction and magnitude of change varying strongly by quarter and intensifying under SSP5-8.5 compared to SSP2-4.5. These patterns reflect biologically significant warming that alters the alignment between local temperatures, vector performance, and parasite development rather than producing a uniform increase in transmission risk throughout the year. *Phlebotomus papatasi* is the primary vector of *L. major*, and both its development and survival across life stages are strongly temperature dependent (Bozorg-Omid et al., 2025; Charrahy et al., 2022). Parasite development within the vector, expressed through EIP, is likewise temperature sensitive, with accelerated development at higher temperatures but constrained by sublethal and lethal thresholds (Bates, 2007; Quiñonez-Díaz et al., 2012).

Consistent with these thermal constraints, projected mid-century changes at endemic sites reveal marked seasonal asymmetry, suggesting most regions are heading in the direction of optimal or near-optimal temperatures for sand fly as well as the parasite (Bounoua et al., 2013; Charrahy et al., 2022; Colacicco-Mayhugh et al., 2010). Suitability increases substantially during Q1 under both SSP2-4.5 and SSP5-8.5, reflecting relaxation of cold limitations early in the transmission season. In contrast, Q2 and Q3 exhibit pronounced and highly consistent declines in suitability across endemic locations, with effect sizes approaching −1, indicating that warming during peak summer months increasingly exceeds optimal conditions for vector survival and effective parasite development. Changes during Q4 are comparatively modest and scenario-dependent. These results indicate that climate change is likely to redistribute transmission potential seasonally, concentrating risk earlier

in the year while suppressing it during the hottest months, rather than uniformly amplifying suitability across all seasons.

Under SSP5-8.5, stronger warming intensifies these seasonal shifts, producing larger departures from present-day suitability than under SSP2-4.5. While modest gains persist in cooler quarters, small but consistent reductions in suitability under high-emissions scenarios likely reflect upper thermal limits to adult survival and fecundity, consistent with experimental and field evidence showing abrupt fitness declines in *P. papatasi* beyond 35 °C (El Omari et al., 2020; Gherbi et al., 2020; Hanafi-Bojd et al., 2015). These findings highlight the fragile thermal boundaries that delimit the transmission niche and emphasize that warming can both enhance and constrain risk depending on seasonal context.

The statistically significant differences between SSP5-8.5 and SSP2-4.5 underscore that climate change does not simply expand suitable areas geographically but modifies the efficiency and timing of transmission by altering key components of *VC*, particularly survival and EIP duration. Consequently, outbreaks may become more temporally concentrated or episodic rather than continuously elevated, even in the absence of range expansion (Hanafi-Bojd et al., 2015). This seasonal restructuring of risk reinforces the need for adaptive surveillance and vector control strategies that account for when, not only where, transmission is biologically feasible. Hence, underlying the need for adaptive surveillance and vector control interventions to take account not only of vector presence but also of changing thermal performance landscapes. Finally, by using a mechanistic modeling framework integrating life history and VC, we can move beyond static correlative models. By translating the biological drivers of transmission into a framework, it provides a process-based approach to anticipate disease behavior under climate change, especially in environmentally marginal but biologically permissive locations (Buckingham-Jeffery et al., 2019; Miller et al., 2014).

In addition, our uncertainty-propagated projections demonstrate that biological uncertainty is itself strongly seasonal. While posterior mean projections closely resemble deterministic estimates, uncertainty envelopes widen substantially during warm-season quarters, particularly Q2 and Q3, where nonlinear temperature responses amplify sensitivity to trait parameter variation. These patterns reflect parametric uncertainty in temperature-dependent survival, development, and biting rates, as well as external uncertainty arising from climate projections (Lagerwall et al., 2014; Rigosi & Rueda, 2012; Rounsevell et al., 2021). Importantly, uncertainty does not obscure the dominant seasonal signal: even under favorable biological assumptions, suitability consistently declines during peak summer at endemic sites, reinforcing the robustness of the observed seasonal redistribution. By explicitly propagating trait-level uncertainty, our framework moves beyond deterministic future risk mapping and provides a more realistic representation of confidence bounds around projected transmission suitability, an approach rarely implemented for cutaneous leishmaniasis despite its relevance for decision-making under climate change.

4.3. Climate suitability and health care access

One of the most important and underappreciated aspects of vector-borne disease risk is the spatial correspondence between transmission hazard and public health capacity (Talisuna et al., 2020). Our analysis of *L. major* climatic suitability and distance to healthcare facilities indicates a moderate but statistically significant positive association under present-day climate conditions, with many areas of elevated ZCL risk also being relatively poorly served by healthcare infrastructure (Ahmed et al., 2020; Carlson et al., 2022; Du et al., 2016; Talisuna et al., 2020). This relationship persists across population-masked domains and strengthens systematically as the analysis is restricted to increasingly inhabited areas, indicating that climatic suitability and healthcare access constraints are not randomly distributed in space.

The public health implications of this co-location are substantial. Small increases in climatic suitability within resource-constrained regions may result in disproportionately large health impacts, mediated by delayed diagnosis, low disease awareness, and limited access to antileishmanial treatment. Even under current climatic conditions, the interaction between heightened ecological suitability and compromised health systems creates a synergistic risk environment, in which localized outbreaks may remain undetected or inadequately controlled. Consequently, exposure to climate-driven ZCL risk is not solely an environmental process but also reflects underlying socio-spatial inequities in health system access (Ahmed et al., 2020; Carlson et al., 2022; Talisuna et al., 2020).

Sensitivity analyses conditioning on population density reveals a clear and monotonic strengthening of the suitability–healthcare association as the analysis focuses on more densely populated areas (Table 5). At low population thresholds (≥1 person km^{-2}), the relationship is positive but moderate, reflecting heterogeneous co-location patterns across sparsely inhabited landscapes. As population thresholds increase, correlation strength rises steadily, with Pearson coefficients exceeding 0.4 beyond ≥25 persons km^{-2} and reaching 0.50 (95% CI: 0.49–0.52) at ≥100 persons km^{-2}. This progressive intensification indicates that in highly populated settings, where disease burden is likely to be greatest, areas of high climatic suitability increasingly coincide with limited healthcare accessibility. Narrowing confidence intervals at higher thresholds further indicates improved statistical stability as analyses focus on core inhabited domains.

These spatial patterns are consistent with biological expectations. *Phlebotomus papatasi* is well adapted to hot, dry environments characterized by sparse vegetation and limited shelter, conditions that often overlap with peripheral or underserved regions of health system coverage (El Omari et al., 2020; Gherbi et al., 2020; Hanafi-Bojd et al., 2015). As climatic suitability expands or intensifies within such settings, transmission risk is likely to increase in areas least equipped to support timely detection and treatment, amplifying vulnerability beyond what would be inferred from environmental suitability alone.

The bivariate classification of climatic suitability and healthcare accessibility further illustrates these inequities (Figure 7). Large contiguous zones of high suitability combined with poor healthcare access are concentrated across inland and arid regions of southern Morocco, central and southern Algeria, interior Libya, and parts of western and southern Egypt. These regions represent priority areas where elevated ecological risk and structural health system constraints converge. Areas of high suitability but moderate to good healthcare access are more spatially restricted and largely confined to coastal and peri-urban settings, while low suitability with good access predominates along densely populated coastal corridors and major urban centers.

Intermediate combinations, particularly moderate suitability paired with poor or moderate access, form extensive transitional belts surrounding high-risk zones. These areas are especially sensitive to incremental changes in either climate suitability or healthcare infrastructure, such that relatively small shifts could substantially alter local vulnerability profiles. Together, these results underscore the importance of integrating climate-based risk projections with spatial assessments of healthcare capacity to identify locations where climate change may exacerbate existing health inequities.

Moreover, to effectively mitigate future ZCL outbreaks, surveillance and intervention strategies must therefore account for overlapping ecological and infrastructural risks, rather than treating climatic suitability in isolation. Integrating climate-driven suitability maps with healthcare accessibility assessments enables more targeted prioritization of mobile diagnostics, community-based surveillance, and resource allocation in regions where rising ecological risk coincides with limited capacity for timely response.

4.4. Limitations

Despite its strengths, this study has two main limitations that warrant consideration. First, although we used ensemble-mean climate projections and explicitly propagated temperature-driven biological uncertainty using Monte Carlo simulations, uncertainty in future climate forcing, particularly at seasonal scales, remains an important source of external uncertainty that could influence projected suitability patterns (Rounsevell et al., 2021). Ensemble means provide robust central tendencies, but they may obscure extremes or inter-model variability that could become epidemiologically relevant under high-emissions scenarios.

Second, our analysis focuses on a mid-century climate horizon (circa 2050) to balance decision relevance with the emergence of a clear climate signal. While appropriate for strategic planning, future work could extend this framework using multi-horizon analyses or scenario ensembles to better characterize longer-term uncertainty trajectories. Nevertheless, compared to highly data-intensive epidemic modeling frameworks that require detailed demographic and intervention data, our trait-based, mechanistic approach, combined with explicit uncertainty propagation, offers a pragmatic and interpretable tool for neglected tropical diseases where data scarcity remains a central constraint.

5. Conclusion

This study presents a biologically grounded yet operationally simple framework for assessing the climate-driven transmission risk of ZCL mediated by *P. papatasi*. By integrating temperature-sensitive life history traits with *VC* metrics within the rodent suitability envelope, and explicitly propagating biological uncertainty through Monte Carlo simulations, we generate composite suitability indices that capture both the magnitude and seasonal structure of present-day and future transmission risk under plausible climate scenarios. Our results show that while many currently endemic areas remain ecologically below critical transmission thresholds, projected climate change is likely to induce pronounced and seasonally heterogeneous shifts in suitability, with the strongest and most consistent changes occurring during the first three quarters of the year and under high-emissions scenarios.

Importantly, future climatic risk does not increase uniformly across space or seasons. Paired site-level analyses reveal near-uniform directional shifts in suitability across endemic locations in Q1–Q3, whereas late-season changes are comparatively modest and scenario dependent. These findings underscore that climate change is likely to alter not only the intensity but also the seasonal timing of ZCL transmission potential, with implications for surveillance calendars and early warning systems. The close agreement between deterministic projections and posterior mean estimates further indicates that broad spatial risk patterns are robust, while uncertainty bounds highlight where nonlinear thermal responses may amplify or constrain transmission under alternative biological assumptions.

At the same time, our bivariate analysis demonstrates that predicted climatic suitability increasingly overlaps with gradients in healthcare accessibility, revealing priority zones where elevated ecological risk coincides with limited health system access. Together, these results highlight the need for integrated preparedness strategies that explicitly combine climate-informed transmission risk with health system capacity assessments. Targeted investments in mobile diagnostics, community-based surveillance, and adaptive planning that accounts for seasonal risk concentration will be essential to ensuring timely detection and mitigation of ZCL under a warming climate.

Supplementary Material

The Supplementary Material can be found online at: https://sesmo.org/article/view/18934/xxx.

Funding

This work received financial support from the following project: Advancing Disease Modeling with ICIPE & ACDI Expertise. Project grant number 125001; the Swedish International Development Cooperation Agency (Sida); the Swiss Agency for Development and Cooperation (SDC); the Australian Centre for International Agricultural Research (ACIAR); the Norwegian Agency for Development Cooperation (Norad); the German Federal Ministry for Economic Cooperation and Development (BMZ); and the Government of the Republic of Kenya. The views expressed herein do not necessarily reflect the official opinion of the donors. The authors also acknowledge Harriet Wambui Wangu for her contributions during the mapping process.

CRediT

Komi Mensah Agboka: Writing – review & editing, Writing – original draft, Visualization, Validation, Supervision, Software, Methodology, Investigation, Formal analysis, Conceptualization. Souleymane Diallo: Writing – original draft, Writing – review & editing. Steve Baleba: Writing – review & editing. Iman Brema Hassaballa: Writing – review & editing. Quinto Meltus Juma: Data curation, Visualization. Allan Muohi Ngángá: Data curation. Harriet Wambui Wangu: data curation. Khalid Ahmed: Writing – review & editing. Chrysantus M. Tanga: Writing – review & editing. Tobias Landmann: Writing – review & editing, Supervision. Elfatih Abdel-Rahman: Writing – review & editing, Supervision.

References

Agboka, K.M., Diallo, S., Hassaballa, I.B., Meltus, Q.J., Ahmed, K., Tanga, C.M., Landmann, T., & Abdel-Rahman, E.M. (2026) Temperature-and host-driven model of Phlebotomus papatasi outbreak potential under climate change in Sudan. Ecological Modelling 511, 111386. https://doi.org/10.1016/j.ecolmodel.2025.111386.

Agboka, K.M., Ndjomatchoua, F.T., Guimapi, R.A., Rossini, L., Azrag, A.G.A., Meltus, Q.J., Landmann, T., Ekesi, S., & Abdel-Rahman, E.M. (2025a) Dual Perspectives From Mechanistic and Correlative Approaches in Mapping the Distribution of the Lesser Mealworm Alphitobius diaperinus. Physiol Plant. 177(6), e70659. doi: 10.1111/ppl.70659. PMID: 41320850.

Agboka, K. M., Ndjomatchoua, F. T., Rossini, L., Guimapi, R. A., & Abdel-Rahman, E. M. (2025b). When thermal risk indices work and when they don't: A case study of two maize insect pests. MethodsX, 15, 103537. https://doi.org/10.1016/j.mex.2025.103537.

Ahmed, A., Ali, Y., & Mohamed, N. S. (2020). Arboviral diseases: the emergence of a major yet ignored public health threat in Africa. The Lancet. Planetary health, 4(12), e555. https://doi.org/10.1016/S2542-5196(20)30269-2.

Aoun, K., & Bouratbine, A. (2014). Cutaneous leishmaniasis in North Africa: a review. Parasite (Paris, France), 21, 14. https://doi.org/10.1051/parasite/2014014.

Babaousmail, H., Hou, R., Ayugi, B., Ojara, M., Ngoma, H., Karim, R., Rajasekar, A., & Ongoma, V. (2021). Evaluation of the Performance of CMIP6 Models in Reproducing Rainfall Patterns over North Africa. Atmosphere, 12(4), 475. https://doi.org/10.3390/atmos12040475.

Bates P. A. (2007). Transmission of Leishmania metacyclic promastigotes by phlebotomine sand flies. International journal for parasitology, 37(10), 1097–1106. https://doi.org/10.1016/j.ijpara.2007.04.003.

Benkova, I., & Volf, P. (2007). Effect of temperature on metabolism of Phlebotomus papatasi (Diptera: Psychodidae). Journal of medical entomology, 44(1), 150–154. https://doi.org/10.1603/0022-2585(2007)44[150:eotomo]2.0.co;2.

Berry, I., & Berrang-Ford, L. (2016). Leishmaniasis, conflict, and political terror: A spatio-temporal analysis. Social Science & Medicine, 167, 140-149.

Bounoua, L., Kahime, K., Houti, L., Blakey, T., Ebi, K. L., Zhang, P., Imhoff, M. L., Thome, K. J., Dudek, C., Sahabi, S. A., Messouli, M., Makhlouf, B., El Laamrani, A., & Boumezzough, A. (2013). Linking climate to incidence of zoonotic cutaneous leishmaniasis (L. major) in pre-Saharan North Africa. International journal of environmental research and public health, 10(8), 3172–3191. https://doi.org/10.3390/ijerph10083172.

Bozorg-Omid, F., Youssefi, F., Hassanpour, G., Rahimi Foroushani, A., Rahimi, M., Shirzadi, M. R., Jafari, R., & Hanafi-Bojd, A. A. (2025). Predicting the Effect of Temperature Changes on Phlebotomus papatasi Activity, as the Main Vector of Zoonotic Cutaneous Leishmaniasis in Iran. Transboundary and emerging diseases, 2025, 9518371. https://doi.org/10.1155/tbed/9518371.

Brady, O. J., Godfray, H. C., Tatem, A. J., Gething, P. W., Cohen, J. M., McKenzie, F. E., Perkins, T. A., Reiner, R. C., Jr, Tusting, L. S., Sinka, M. E., Moyes, C. L., Eckhoff, P. A., Scott, T. W., Lindsay, S. W., Hay, S. I., & Smith, D. L. (2016). Vectorial capacity and vector control: reconsidering sensitivity to parameters for malaria elimination. Transactions of the Royal Society of Tropical Medicine and Hygiene, 110(2), 107–117. https://doi.org/10.1093/trstmh/trv113.

Buckingham-Jeffery, E., Hill, E. M., Datta, S., Dilger, E., & Courtenay, O. (2019). Spatio-temporal modelling of Leishmania infantum infection among domestic dogs: a simulation study and sensitivity analysis applied to rural Brazil. Parasites & vectors, 12(1), 215. https://doi.org/10.1186/s13071-019-3430-y.

Carlson, C. J., Albery, G. F., Merow, C., Trisos, C. H., Zipfel, C. M., Eskew, E. A., Olival, K. J., Ross, N., & Bansal, S. (2022). Climate change increases cross-species viral transmission risk. Nature, 607(7919), 555–562. https://doi.org/10.1038/s41586-022-04788-w.

Ceccato, P., Vancutsem, C., Klaver, R., Rowland, J., & Connor, S. J. (2012). A vectorial capacity product to monitor changing malaria transmission potential in epidemic regions of Africa. Journal of tropical medicine, 2012, 595948. https://doi.org/10.1155/2012/595948.

Chamberlain, S. A., & Boettiger, C. (2017). R Python, and Ruby clients for GBIF species occurrence data. PeerJ Preprints.

Charrahy, Z., Yaghoobi-Ershadi, M. R., Shirzadi, M. R., Akhavan, A. A., Rassi, Y., Hosseini, S. Z., Webb, N. J., Haque, U., Bozorg Omid, F., & Hanafi-Bojd, A. A. (2022). Climate change and its effect on the vulnerability to zoonotic cutaneous leishmaniasis in Iran. Transboundary and emerging diseases, 69(3), 1506–1520. https://doi.org/10.1111/tbed.14115.

Chelbi, I., & Zhioua, E. (2007). Biology of Phlebotomus papatasi (Diptera: Psychodidae) in the laboratory. Journal of medical entomology, 44(4), 597–600. https://doi.org/10.1603/0022-2585(2007)44[597:boppdp]2.0.co;2.

Colacicco-Mayhugh, M. G., Masuoka, P. M., & Grieco, J. P. (2010). Ecological niche model of Phlebotomus alexandri and P. papatasi (Diptera: Psychodidae) in the Middle East. International journal of health geographics, 9, 2. https://doi.org/10.1186/1476-072X-9-2.

Dennington, N. L., Grossman, M. K., Ware-Gilmore, F., Teeple, J. L., Johnson, L. R., Shocket, M. S., McGraw, E. A., & Thomas, M. B. (2024). Phenotypic adaptation to temperature in the mosquito vector, Aedes aegypti. Global change biology, 30(1), e17041. https://doi.org/10.1111/gcb.17041.

Diekmann, O., Heesterbeek, J. A., & Metz, J. A. (1990). On the definition and the computation of the basic reproduction ratio R0 in models for infectious diseases in heterogeneous populations. Journal of mathematical biology, 28(4), 365–382. https://doi.org/10.1007/BF00178324.

Du, R., Hotez, P. J., Al-Salem, W. S., & Acosta-Serrano, A. (2016). Old World Cutaneous Leishmaniasis and Refugee Crises in the Middle East and North Africa. PLoS neglected tropical diseases, 10(5), e0004545. https://doi.org/10.1371/journal.pntd.0004545.

El Omari, H., Chahlaoui, A., Talbi, F. Z., Mouhdi, K. E., & El Ouali Lalami, A. (2020). Impact of Climatic Factors on the Seasonal Fluctuation of Leishmaniasis Vectors in Central Morocco (Meknes Prefecture). The Canadian journal of infectious diseases & medical microbiology = Journal canadien des maladies infectieuses et de la microbiologie medicale, 2020, 6098149. https://doi.org/10.1155/2020/6098149.

Fick, S.E. and Hijmans, R.J. (2017), WorldClim 2: new 1-km spatial resolution climate surfaces for global land areas. Int. J. Climatol, 37: 4302-4315. https://doi.org/10.1002/joc.5086.

Garrett-Jones C. (1964). Prognosis for interruption of malaria transmission through assessment of the mosquito's vectorial capacity. Nature, 204, 1173–1175. https://doi.org/10.1038/2041173a0.

Gherbi, R., Bounechada, M., Latrofa, M. S., Annoscia, G., Tarallo, V. D., Dantas-Torres, F., & Otranto, D. (2020). Phlebotomine sand flies and Leishmania species in a focus of cutaneous leishmaniasis in Algeria. PLoS neglected tropical diseases, 14(2), e0008024. https://doi.org/10.1371/journal.pntd.0008024.

Halimi, M., Cheghabaleki, Z. Z., Modrek, M. J., & Delavari, M. (2016). Temporal Dynamics of Phlebotomine Sand Flies Population in Response to Ambient Temperature Variation, Bam, Kerman Province of Iran. Annals of global health, 82(5), 824–831. https://doi.org/10.1016/j.aogh.2016.07.009.

Hanafi-Bojd, A. A., Yaghoobi-Ershadi, M. R., Haghdoost, A. A., Akhavan, A. A., Rassi, Y., Karimi, A., & Charrahy, Z. (2015). Modeling the Distribution of Cutaneous Leishmaniasis Vectors (Psychodidae: Phlebotominae) in Iran: A Potential Transmission in Disease Prone Areas. Journal of medical entomology, 52(4), 557–565. https://doi.org/10.1093/jme/tjv058.

Hand D. J. (2007). Principles of data mining. Drug safety, 30(7), 621–622. https://doi.org/10.2165/00002018-200730070-00010.

Hengl T, Heuvelink GBM, Kempen B, Leenaars JGB, Walsh MG, et al. (2015) Mapping Soil Properties of Africa at 250 m Resolution: Random Forests Significantly Improve Current Predictions. PLOS ONE 10(6): e0125814. https://doi.org/10.1371/journal.pone.0125814.

Hotez, P. J., Savioli, L., & Fenwick, A. (2012). Neglected tropical diseases of the Middle East and North Africa: review of their prevalence, distribution, and opportunities for control. PLoS neglected tropical diseases, 6(2), e1475. https://doi.org/10.1371/journal.pntd.0001475.

Hou, H., Zhou, B.-B., Pei, F., Hu, G., Su, Z., Zeng, Y., et al. (2022). Future land use/land cover change has nontrivial and potentially dominant impact on global gross primary productivity. Earth's Future, 10, e2021EF002628. https://doi.org/10.1029/2021EF002628.

Hua, R., Su, Q., Fan, J., Wang, L., Xu, L., Hui, Y., Huang, M., Du, B., Tian, Y., Zhao, Y., & Manduriwa (2025). Temporal and Spatial Dynamics of Rodent Species Habitats in the Ordos Desert Steppe, China. Animals : an open access journal from MDPI, 15(5), 721. https://doi.org/10.3390/ani15050721.

Huete, A., Justice, C., & Van Leeuwen, W. (1999). MODIS vegetation index (MOD13). Algorithm theoretical basis document, 3(213), 295-309.

Karmaoui, A., Sereno, D., El Jaafari, S., & Hajji, L. (2022a). Seasonal patterns of zoonotic cutaneous leishmaniasis caused by L. major and transmitted by Phlebotomus papatasi in the North Africa region, a systematic review and a meta-analysis. Microorganisms, 10(12), 2391.

Karmaoui, A., Ben Salem, A., Sereno, D., El Jaafari, S., & Hajji, L. (2022b). Geographic distribution of Meriones shawi,Psammomys obesus, and Phlebotomus papatasi the main reservoirs and principal vector of zoonotic cutaneous leishmaniasis in the Middle East and North Africa. Parasite epidemiology and control, 17, e00247. https://doi.org/10.1016/j.parepi.2022.e00247.

Kasap, O. E., & Alten, B. (2005). Laboratory estimation of degree-day developmental requirements of Phlebotomus papatasi (Diptera: Psychodidae). Journal of vector ecology : journal of the Society for Vector Ecology, 30(2), 328–333.

Lagerwall, G., Kiker, G., Muñoz-Carpena, R., & Wang, N. (2014). Global uncertainty and sensitivity analysis of a spatially distributed ecological model. Ecological modelling, 275, 22-30. https://doi.org/10.1016/j.ecolmodel.2013.12.010.

Lawyer, P. G., Githure, J. I., Anjili, C. O., Olobo, J. O., Koech, D. K., & Reid, G. D. (1990). Experimental transmission of Leishmania major to vervet monkeys (Cercopithecus aethiops) by bites of Phlebotomus duboscqi (Diptera: Psychodidae). Transactions of the Royal Society of Tropical Medicine and Hygiene, 84(2), 229–232. https://doi.org/10.1016/0035-9203(90)90266-h.

Macdonald. G, M. G. (1957). The epidemiology and control of malaria.

Miller, E., Warburg, A., Novikov, I., Hailu, A., Volf, P., Seblova, V., & Huppert, A. (2014). Quantifying the contribution of hosts with different parasite concentrations to the transmission of visceral leishmaniasis in Ethiopia. PLoS neglected tropical diseases, 8(10), e3288. https://doi.org/10.1371/journal.pntd.0003288.

Mordecai, E. A., Caldwell, J. M., Grossman, M. K., Lippi, C. A., Johnson, L. R., Neira, M., Rohr, J. R., Ryan, S. J., Savage, V., Shocket, M. S., Sippy, R., Stewart Ibarra, A. M., Thomas, M. B., & Villena, O. (2019). Thermal biology of mosquito-borne disease. Ecology letters, 22(10), 1690–1708. https://doi.org/10.1111/ele.13335.

Ndjomatchoua, F. T., Guimapi, R. A. Y., Rossini, L., Djouda, B. S., & Pedro, S. A. (2024). A generalized risk assessment index for forecasting insect population under the effect of temperature. Journal of thermal biology, 122, 103886. https://doi.org/10.1016/j.jtherbio.2024.103886.

Parham, P. E., & Michael, E. (2010). Modelling climate change and malaria transmission. Advances in experimental medicine and biology, 673, 184–199. https://doi.org/10.1007/978-1-4419-6064-1_13.

Parkash V, Ashwin H, Sadlova J, Vojtkova B, Jones G, Martin N, Greensted E, Allgar V, Kamhawi S, Valenzuela JG, Layton AM, Jaffe CL, Volf P, Kaye PM, Lacey CJN. A clinical study to optimise a sand fly biting protocol for use in a controlled human infection model of cutaneous leishmaniasis (the FLYBITE study). Wellcome Open Res. 2021 Jun 30;6:168. doi: 10.12688/wellcomeopenres.16870.1. PMID: 34693027; PMCID: PMC8506224.

Quiñonez-Díaz, L., Mancilla-Ramírez, J., Avila-García, M., Ortiz-Avalos, J., Berron, A., González, S., Paredes, Y., & Galindo-Sevilla, N. (2012). Effect of ambient temperature on the clinical manifestations of experimental diffuse cutaneous leishmaniasis in a rodent model. Vector borne and zoonotic diseases (Larchmont, N.Y.), 12(10), 851–860. https://doi.org/10.1089/vbz.2011.0844.

R Core Team. (2025). R Foundation for Statistical Computing, Vienna, Austria.

Rigosi, A., & Rueda, F. J. (2012). Propagation of uncertainty in ecological models of reservoirs: From physical to population dynamic predictions. Ecological Modelling, 247, 199-209.https://doi.org/10.1016/j.ecolmodel.2012.08.022.

Rizzoli, A., Tagliapietra, V., Cagnacci, F., Marini, G., Arnoldi, D., Rosso, F., & Rosà, R. (2019). Parasites and wildlife in a changing world: The vector-host- pathogen interaction as a learning case. International journal for parasitology. Parasites and wildlife, 9, 394–401. https://doi.org/10.1016/j.ijppaw.2019.05.011.

Rossini, L., & Bruzzone, O. A. (2025). A novel PDE model to describe terrestrial arthropods considering physiological age, reproduction rate, and body mass. Acta IMEKO, 14(1), 1-11. https://doi.org/10.21014/actaimeko.v14i1.1873.

Rossini, L., Bruzzone, O. A., Contarini, M., Bufacchi, L., & Speranza, S. (2022). A Physiologically Based ODE Model for an Old Pest: Modeling Life Cycle and Population Dynamics of Bactrocera oleae (Rossi). Agronomy, 12(10), 2298. https://doi.org/10.3390/agronomy12102298.

Rossini, L., Contarini, M., Bono Rosselló, N., Garone, E., & Speranza, S. (2022, September). Prediction of infestations by true bugs in hazelnut orchards: feasibility and preliminary approaches in the case of Halyomorpha halys. In X International Congress on Hazelnut 1379 (pp. 463-472). https://doi.org/10.17660/ActaHortic.2023.1379.66.

Rossini, L., Contarini, M. & Speranza, S. A novel version of the Von Foerster equation to describe poikilothermic organisms including physiological age and reproduction rate. Ricerche mat **70**, 489–503 (2021). https://doi.org/10.1007/s11587-020-00489-6.

Rossini, L., Contarini, M., Speranza, S., Mermer, S., Walton, V., Francis, F., & Garone, E. (2024). Life tables in entomology: A discussion on tables' parameters and the importance of raw data. PloS one, 19(3), e0299598. https://doi.org/10.1371/journal.pone.0299598.

Rossini, L., Lots, A., Noël, G., Segers, A., Mermer, S., Contarini, M., Speranza, S., Walton, V., Francis, F., & Garone, E. (2025). Life tables data collection in entomology: an overview on the differential and the integral representation and proposal for a standard electronic file. Insect science, 10.1111/1744-7917.70040. Advance online publication. https://doi.org/10.1111/1744-7917.70040.

Rossini, L., Rosselló, N. B., Contarini, M., Speranza, S., & Garone, E. (2022). Modelling ectotherms' populations considering physiological age structure and spatial motion: A novel approach. Ecological Informatics, 70, 101703. https://doi.org/10.1016/j.ecoinf.2022.101703.

Rossini, L., Severini, M., Contarini, M., & Speranza, S. (2019). A novel modelling approach to describe an insect life cycle vis-à-vis plant protection: description and application in the case study of Tuta absoluta. Ecological Modelling, 409, 108778. https://doi.org/10.1016/j.ecolmodel.2019.108778.

Rounsevell, M. D., Arneth, A., Brown, C., Cheung, W. W., Gimenez, O., Holman, I., ... & Shin, Y. J. (2021). Identifying uncertainties in scenarios and models of socio-ecological systems in support of decision-making. One Earth, 4(7), 967-985. https://doi.org/10.1016/j.oneear.2021.06.003.

Suh, E., Grossman, M. K., Waite, J. L., Dennington, N. L., Sherrard-Smith, E., Churcher, T. S., & Thomas, M. B. (2020). The influence of feeding behaviour and temperature on the capacity of mosquitoes to transmit malaria. Nature ecology & evolution, 4(7), 940–951. https://doi.org/10.1038/s41559-020-1182-x.

Talisuna, A. O., Okiro, E. A., Yahaya, A. A., Stephen, M., Bonkoungou, B., Musa, E. O., Minkoulou, E. M., Okeibunor, J., Impouma, B., Djingarey, H. M., Yao, N. K. M., Oka, S., Yoti, Z., & Fall, I. S. (2020). Spatial and temporal distribution of infectious disease epidemics, disasters and other potential public health emergencies in the World Health Organisation Africa region, 2016-2018. Globalization and health, 16(1), 9. https://doi.org/10.1186/s12992-019-0540-4.

Terradas, G., Manzano-Alvarez, J., Vanalli, C., Werling, K., Cattadori, I. M., & Rasgon, J. L. (2024). Temperature affects viral kinetics and vectorial capacity of Aedes aegypti mosquitoes co-infected with Mayaro and Dengue viruses. Parasites & vectors, 17(1), 73. https://doi.org/10.1186/s13071-023-06109-0.

Thompson, R. N., Gilligan, C. A., & Cunniffe, N. J. (2020). Will an outbreak exceed available resources for control? Estimating the risk from invading pathogens using practical definitions of a severe epidemic. Journal of the Royal Society, Interface, 17(172), 20200690. https://doi.org/10.1098/rsif.2020.0690.

van den Driessche, P., & Watmough, J. (2002). Reproduction numbers and sub-threshold endemic equilibria for compartmental models of disease transmission. Mathematical biosciences, 180, 29–48. https://doi.org/10.1016/s0025-5564(02)00108-6.

Wilson, A. J., Morgan, E. R., Booth, M., Norman, R., Perkins, S. E., Hauffe, H. C., ... & Fenton, A. (2017). What is a vector?. Philosophical Transactions of the Royal Society B: Biological Sciences, 372(1719). https://doi.org/10.1098/rstb.2016.0085.

Woolson, R.F. (2008). Wilcoxon Signed-Rank Test. In Wiley Encyclopedia of Clinical Trials (eds R.B. D'Agostino, L. Sullivan and J. Massaro). https://doi.org/10.1002/9780471462422.eoct979.

World Health Organization. Leishmaniasis Fact Sheet. Geneva: World Health Organization; (2023). [cited 2025 Jun 20]. Available from: https://www.who.int/news-room/fact-sheets/detail/leishmaniasis.

Yaghoobi-Ershadi, M. R., Shirani-Bidabadi, L., Hanafi-Bojd, A. A., Akhavan, A. A., & Zeraati, H. (2007). Colonization and Biology of Phlebotomus papatasi, the Main Vector of Cutaneous Leishmaniasis due to Leishmania major. Iran J Public Health, 36(3), 21–26. https://ijph.tums.ac.ir/index.php/ijph/article/view/1735.

Zomer, R.J., Xu, J. & Trabucco, A. Version 3 of the Global Aridity Index and Potential Evapotranspiration Database. Sci Data **9**, 409 (2022). https://doi.org/10.1038/s41597-022-01493-1.